Improving and Evaluating the Stability of Photovoltaics

by

Travis Yeow

A thesis

presented to the University of Waterloo

in fulfillment of the

thesis requirement for the degree of

Masters of Applied Science

in

Mechanical and Mechatronics Engineering (Nano)

Waterloo, Ontario, Canada, 2019

Authors Declaration

I hereby declare that I am the sole author of this thesis. This is a true copy of the thesis, including any required final revisions, as accepted by my examiners. I understand that my thesis may be made electronically available to the public.

Abstract

Advancements in photovoltaic technologies are hindered by stability and degradation. In silicon photovoltaics, these degradation mechanisms include potential induced degradation (PID) and current-induced degradation (CID), among others. In this thesis, impedance spectroscopy is used to examine passivated emitter and rear cell (PERC) silicon modules with PID and CID. A comparison between control and degraded modules is done to identify key differences in the impedance spectra and determine the extent of the degradation. PID was observed at the module level as a dramatic reduction in shunt resistance, with a small amount of spatial inhomogeneity present in the degradation. It was found that accurate characterization of CID via measurement of the minority carrier lifetime requires a high bias voltage at the module level that exceeds the capabilities of a standard impedance spectrometer. Because of this, CID was also examined at the cell level, where reductions in minority carrier lifetimes could be accurately measured. A correlation between the reduction in minority carrier lifetime due to CID and a reduction in the power conversion efficiency was observed. Thus, the PID and CID mechanisms studied here induce unique changes in the impedance spectroscopy results, making them distinguishable and quantifiable. Finally, the ability to mitigate CID through the use of different silicon wafers and a current induced regeneration process was characterized by impedance spectroscopy.

The stability of emerging photovoltaics, such as those based on a metal halide perovskite light-absorbing film, is also tackled. Atmospheric pressure spatial atomic layered deposition (AP-SALD) is a scalable technique to produce dense, uniform, pinhole free thin films. This is ideal for improving the stability of perovskite devices by preventing the ingress of moisture, which causes degradation of the perovskite film. Tungsten oxide is a transparent semiconductor that is attractive for use as a charge-transporting layer in perovskite photovoltaics. By including a nebulizer and ozone generator in our custom-built AP-SALD system, it was possible to produce tungsten oxide films for the first time by this method. Optimized deposition parameters resulted in hexagonal tungsten oxide, which was characterized then annealed into monoclinic tungsten oxide. The growth rate of this procedure suggests layer-by-layer growth, which is consistent with an ALD growth mode. Due to high deposition temperatures, an inverted p-i-n architecture is required to implement tungsten oxide into a perovskite structure. Preliminary trials at incorporating tungsten oxide address the crystal structure and wettability of the WO_3 film. Further tests are necessary to create a device using WO_3 films fabricated by AP-SALD.

Acknowledgements

I would like to acknowledge Professor Kevin Musselman for accepting me into this group. He has provided support and resources throughout this entire project and has aided me in reaching my goals of publishing and working on new technologies in an applicable field.

I would also like to thank the people in my group that have provided me support. This includes Kissan Mistry and Manfred Kao as they welcomed me when I initially joined the group. A lot of days were spent getting the AP-SALD running. The results of our work exemplify our collaborative efforts.

Kissan Mistry has also assisted in reflectance spectroscopy measurements and fittings. Khaled Ibrahim assisted in Ramen spectroscopy measurements.

Kianoosh Poorkazem, has taught me everything I know about perovskites. Khaled Ibrahim and Alex Jones were also there every step of the way.

Canada Solar Inc. for collaborating with our group and providing resources to completing a study on impedance spectroscopy of silicon photovoltaics.

The remaining group members have all provided insight in my project and have made my MASc a truly enjoyable experience. Thank you, Ming Xiao, Hatameh Asgarimoghaddam, Abdullah Alshehri, Reza Mohammadi, Jhi Loke, Chee Teoh and Ahmed Shahin.

Table of Contents

List of Figures

List of Tables

1.0 Introduction

A global increase in energy demands paired with climate change and depleting natural resources has pushed the advancement of sustainable energy technology. Figure 1 depicts the global electricity landscape and future projections. Currently, 25% of global electricity generation is renewable with solar and wind projected to advance the most [1]. By 2035, half the global power output is expected to be renewable and by 2050 half the global power output is expected to be produced by solar and wind. Among all the available technologies, solar energy presents a clean, low maintenance, renewable energy solution that is easy to install. At 3 x 10^{24} J per year, the sun provides the Earth with more energy in an hour than the world uses in a year [2], [3]. The challenge is harnessing that energy to fulfill the world's needs.

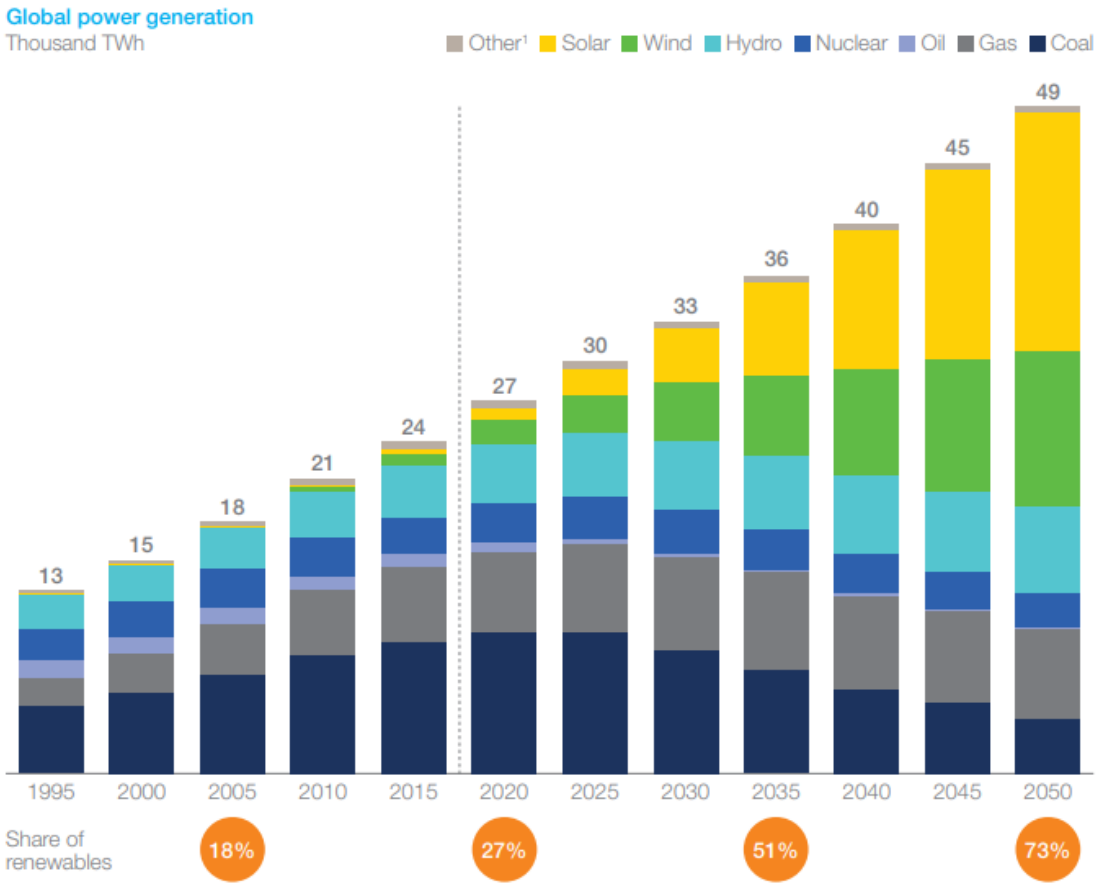

Figure 1: Global energy production and future projections [1]

There are different solar energy technologies designed to harness the power of the sun. The most basic form of this is a solar collector which involves heating a basin of water to generate steam. The steam is used to drive a turbine resulting in electricity. More advanced and efficient technologies known as photovoltaics (PV) directly convert the sun's energy into electricity.

If 0.1% of the Earth's surface or 510,000 km^2 was covered in PV solar panels of 10% efficiency, the world's energy demands could be met [3]. Unfortunately, the cost of solar energy still exceeds coal as seen in Figure 2 [4]. To meet the projections and improve adoption for solar energy, the cost of production must decrease, or the lifetime must increase. This requires new characterization techniques to identify degradation in the solar module which may be used to extend its lifetime [2]. Alternatively, new types of photovoltaic architectures should be investigated apart from the traditional silicon-based technology.

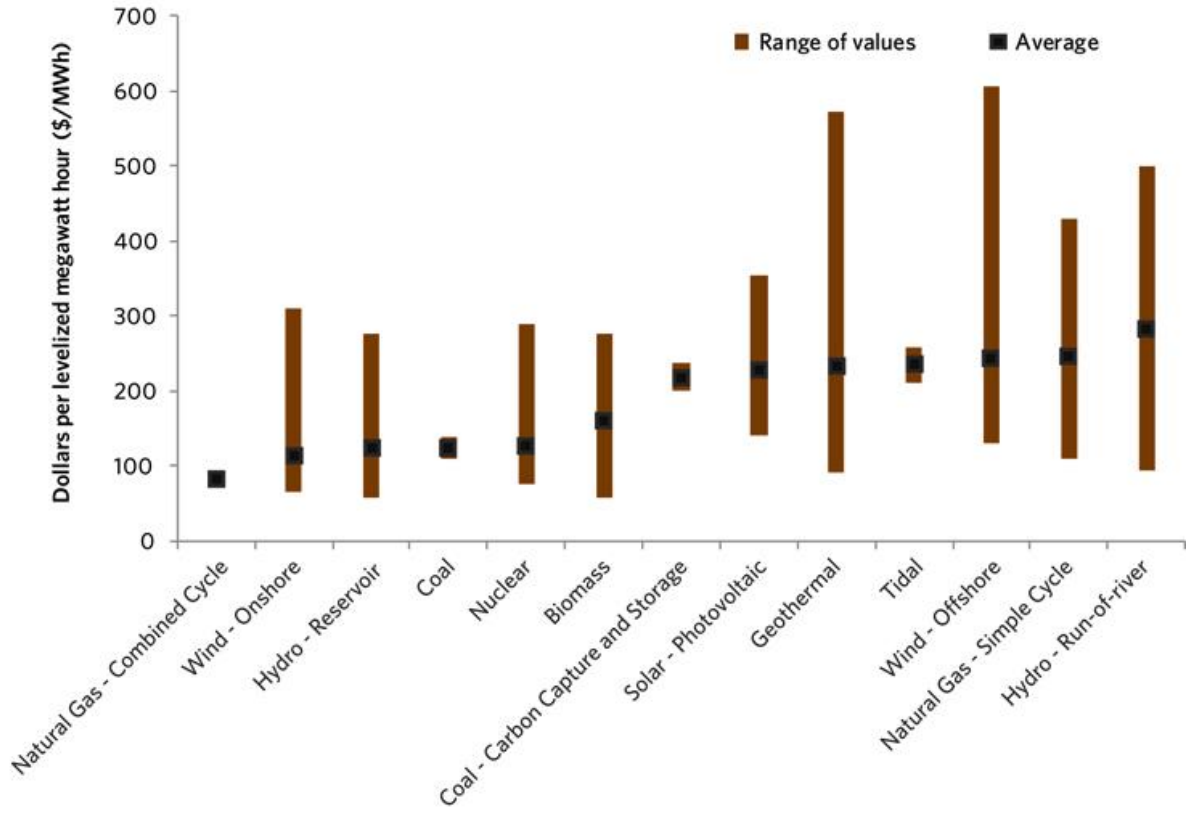

Figure 2: Cost of energy in Canada, 2017 [4]

2.0 Basics of Photovoltaics

2.1 Principles of Solar Operation

In photovoltaic energy conversion, light (photons) travels to the active layer, which is typically a semiconductor, where it is absorbed. The energy excites an electron from the valence band (VB) to the conduction band (CB) of the semiconductor. The minimum energy required for a photon is equivalent to the bandgap of the semiconductor material. This is the energy difference between the valence band and the conduction band. If the photon does not have enough energy, it cannot excite the electron. Prior to excitation, the electron was a part of a covalent bond. After excitation, the network of covalent bonds has one less electron leaving behind a positively charged electron vacancy ("hole") which is propagated by bonded electrons of neighbouring atoms.

An electron conducting (negative or n-type) material and a hole-conducting (positive or p-type) material form an asymmetric junction that separates the excited electrons and holes. Figure 3a illustrates a p-n junction. Pure silicon is neutral and an intrinsic semiconductor. Impurities are added to an intrinsic semiconductor to increase or decrease the number of electrons in the crystal structure in a process known as doping. Intrinsic silicon has four valence electrons all covalently bonded to each other. When boron (containing 3 valence electrons) is added as an impurity, the crystal structure becomes electron deficient leaving a hole in the valence band. This creates a p-type material where the holes are free to move around the crystal lattice. Conversely, phosphorus has 5 valence electrons which results in a surplus of free electrons. When introduced as an impurity in intrinsic silicon, an n-type material is created. In an n-type material, the excess electrons are mobile and carry most of the current making them the majority carrier while holes are the minority carriers.

Since there are a large number of mobile electrons on the n-type side and holes on the p-type side, the electrons from the n-type side begin to diffuse towards the p-type side to fill the holes while the holes in the p-type side diffuse towards the n-type side. This produces negative boron ions in the p-type material while leaving positive phosphorous ions in the n-type material, resulting in the formation of an electric field. This built-in electric field creates a drift current that opposes the diffusion current. At equilibrium (in the dark), the net flow of electrons/holes across the junction is zero. The region where the electric field is located is referred to as the "depletion region" as it is depleted of mobile charges. When light is absorbed by the semiconductor, creating extra electrons and holes, the electric field causes the photogenerated free electrons and holes to migrate towards the n-type or p-type region respectively. Figure 3b shows photogenerated electron-hole pairs in the p-type region drifting to the n-/p-region respectively. These majority carriers (electrons in the n-region and holes in the p-region) eventually recombine through the external circuit creating energy.

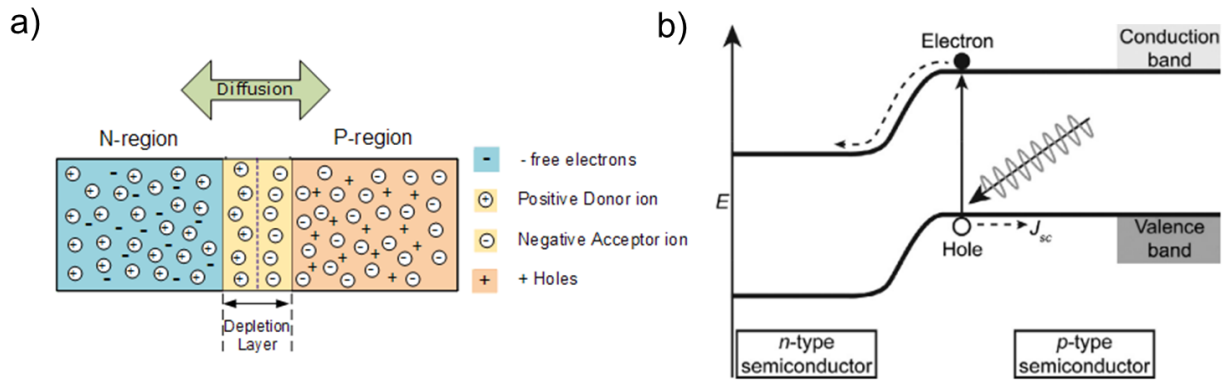

Figure 3: (a) Schematic of p-n junction and (b) energy band diagram [5], [6].

2.2 Photovoltaic Modules

The layers of a typical silicon solar cell can be found in Figure 4a. This consists of a thick p-doped silicon wafer roughly 100 μm thick forming the base of the cell. An n-type layer is

created on top of the n-type layer to form a p-n junction. The surface is textured to be less reflective and enhance light absorption. A SiN_x layer is also added as an anti-reflecting coating and a passivation layer to prevent charges from being trapped at the surface. Silver or aluminum contacts are printed on top of the device and metal contacts at the rear of the device carry charges to an external circuit. Figure 4b illustrates a pattern of metal contacts known as busbars and fingers printed on top of a solar cell which are used to conduct the current generated by a photovoltaic cell. Busbars are used as contact points to wire solar cells together. Fingers are thin contact strips that are perpendicular to busbars which collect the DC generated current and deliver it to busbars.

The single cells are connected in series to form a module as seen in Figure 4c. A module has a higher voltage rating than a single cell. A 12 V module will typically have 36 cells connected in series whereas a 24 V module will have 72 cells connected in series [7]. To be commercially viable, the fragile cells are sandwiched between a transparent front sheet (glass) and a backing sheet (tough plastic). An aluminum frame is fitted around the module to add support.

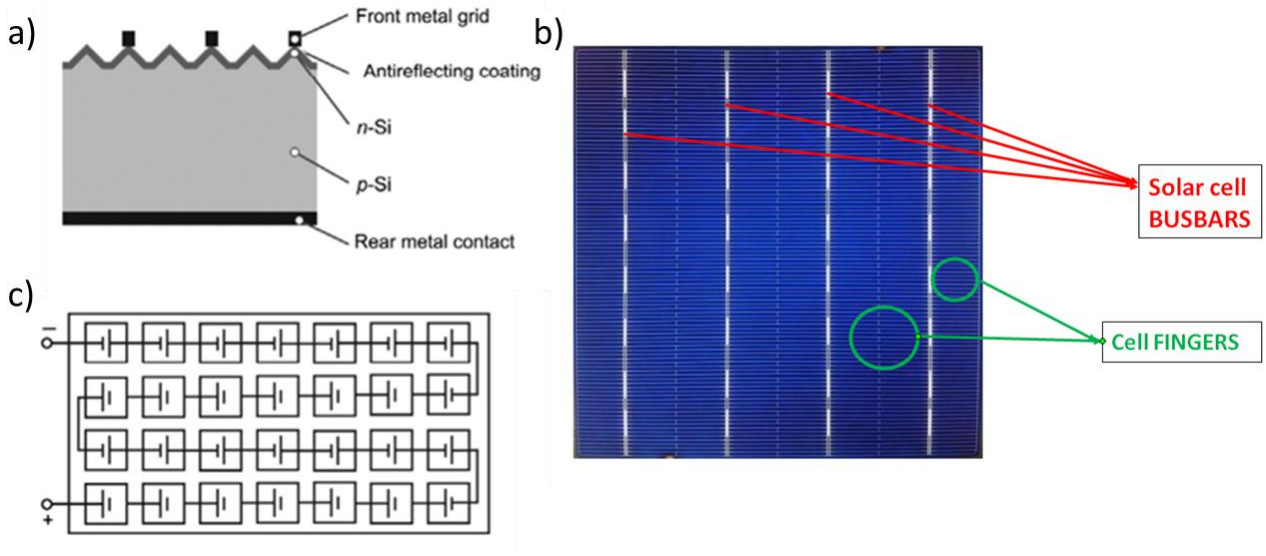

Figure 4: (a) Cross section view of a silicon solar cell, (b) view of a typical solar cell highlighting busbars and fingers and (c) a schematic of a photovoltaic module [5], [8] .

2.3 Measuring the Performance of Solar Cells

There are many methods of measuring the performance of solar cells. The most common method is to measure the power conversion efficiency (PCE). Alternative methods, which provide more information on the properties of the solar cell, include photoluminescence (PL) and electroluminescence (EL) along with impedance spectroscopy.

2.3.1 Power Conversion Efficiency (JV Measurements)

Power conversion efficiency is the most recognized meter of performance in photovoltaics. It is measured by applying a range of voltages to an illuminated cell and measuring the current density. Both current and voltage (and hence power) are produced by the cell in the bottom right quadrant of the current-voltage plot, as shown in Figure 5. The power conversion efficiency (PCE) is defined as the ratio of power delivered to the circuit versus the incident solar power as highlighted by Equation 1.

$$PCE = \frac{P_{out}}{P_{in}} = \frac{FF * J_{SC} * V_{OC}}{P_{in}} = \frac{J_{MP} * V_{MP}}{P_{in}} \quad (1)$$

Where fill factor (FF) is the ratio between the actual power of the cell (P_{Max} in Figure 5) versus the power if there was no series resistance (R_s) and infinite shunt resistance (R_{SH}) (dashed line in Figure 5). Series resistance corresponds to the resistance to current in the junction and electrodes [5]. Shunt paths are alternate pathways within the device caused by defects which reduce the amount of current flowing through the solar cell. A large shunt resistance means there is little to no current leakage. The fill factor is described by equation 2,

$$FF = \frac{J_{MP} * V_{MP}}{J_{SC} * V_{OC}} \quad (2)$$

J_{MP} and V_{MP} are the current density and voltage at maximum power, J_{SC} is the short-circuit current density and V_{OC} is the open circuit voltage, as illustrated in Figure 5.

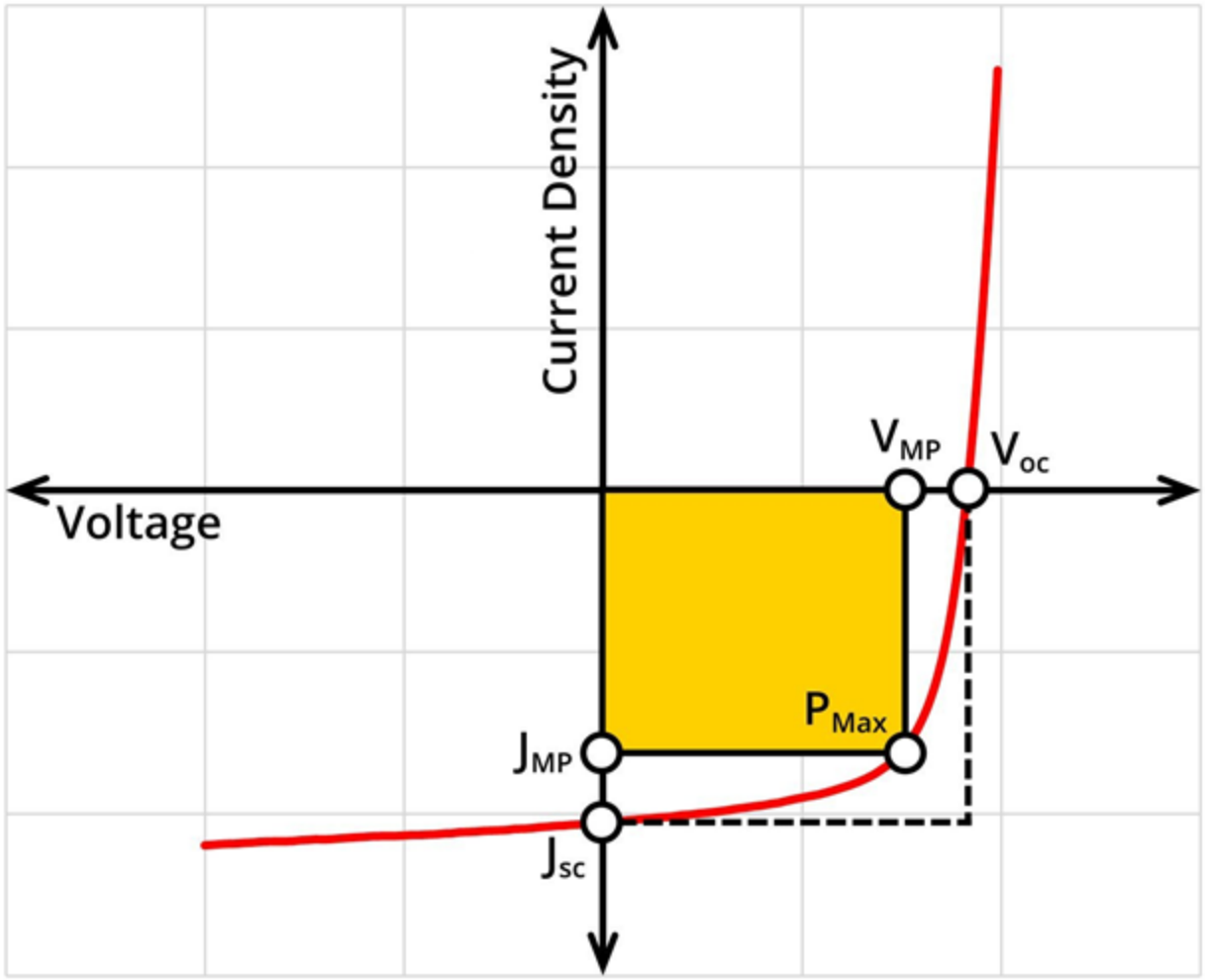

Figure 5: Typical JV curve [9].

When measuring the power conversion efficiency, a standard solar spectrum is used as the incident power. Standard light power used is AM (air mass) 1.5. This corresponds to the relative path length of direct sunlight through the atmosphere with an incident power density of 1000 W/m^2 [10]. In the most ideal case, the fill factor is 1. For most silicon solar cells this value lies around 0.8 [11]. This is indicative of the quality of the solar cell. A low fill factor can indicate diode losses, defects, shunt paths or a high series resistance in the circuit. The greater the fill factor, the greater the PCE will be.

2.3.2 Photoluminescence and Electroluminescence

Photoluminescence and electroluminescence are fast and powerful characterization tools that provide spatially resolved information about the electronic material properties of the solar cells [12]. These techniques use the luminescence phenomenon which is the emission of light by a substance that has not been heated. Photoluminescence involves excitation by external illumination whereas electroluminescence involves applying a voltage bias to the cell [13]. When the solar cell or module is stimulated (excess electrons in the conduction band), radiative recombination of the stimulated electrons in the conduction with holes in the valence band causes light emission, which is measured by a detector. Uniform light emission would be expected from the surface of a homogeneous cell or module, whereas defects appear darker because they dissipate power via non-radiative recombination and hence reveal positions of inhomogeneity [12], [14], [15]. Monocrystalline silicon is ideal for these techniques due to the homogenous nature of the crystal structure. Polycrystalline silicon reveals grain boundaries when examined by EL/PL which may mask defects.

Due to the nature of the excitation, PL can be used on a variety of samples at earlier stages of manufacturing whereas EL is limited to complete cells and modules, as electrical contacts are required. For photovoltaics, EL is more commonly used. A quality solar cell would show uniformity throughout the image. Figure 6 shows a variety of silicon solar cells with various defects. Figure 6(b)-(d) displays defective solar cells that contain small cracks, breaks and finger breaks respectively [16]. Finger breaks alter the ideal current flow path through the metal grid. Defect areas result in a darker region illustrated in the EL image. This technique provides insight into the quality of solar cells by examining and identifying the defects [12], [14], [15].

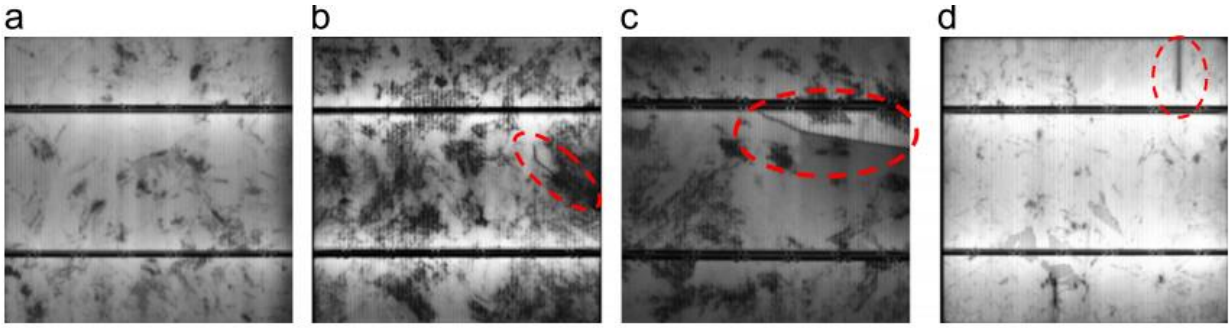

Figure 6: Electroluminescent images of silicon solar cells: a) defect-free, b) small crack, c) break, d) finger-interruption [16].

2.3.3 Impedance Spectroscopy

Impedance spectroscopy is a non-destructive technique that can quantitatively analyze multiple aspects of a photovoltaic's operation. An AC signal of varying frequency is applied over an electrical system, and the real and imaginary impedances are measured at each frequency. These impedances are fit to an equivalent circuit that corresponds to physical features of a solar cell or module [17], [18]. In the case of a silicon solar cell, an equivalent circuit consisting of a series resistor and a resistor and capacitor in parallel, can often be used. A typical Nyquist diagram with this equivalent circuit can be observed in Figure 7, where the x-axis is the real impedance (Z'), the y-axis is the negative of the imaginary impedance (-Z''), and the dotted red line is the impedances measured over a range of frequencies.

Impedance spectroscopy has been used to characterize the series resistance (Rs), parallel resistance (Rp), capacitance (Cp) and time constant (τ) of silicon solar cells under different illumination intensities and temperatures [17], [19]–[21]. These values can translate to the series and shunt resistances, and minority carrier lifetime of the solar cell, which can be used to characterize its quality. The time constant can be determined by the equation:

$$\tau = R_p C_p \quad (3)$$

This is the parallel capacitance multiplied by the parallel resistance and provides a measure of the minority carrier lifetime, i.e. the time a minority carrier exists in an excited state in a cell after electron-hole generation before recombining and losing its energy, typically as heat [17]. As energy should be delivered to the external circuit, rather than lost in the solar cell material, long minority carrier lifetimes, and hence time constants, are desired.

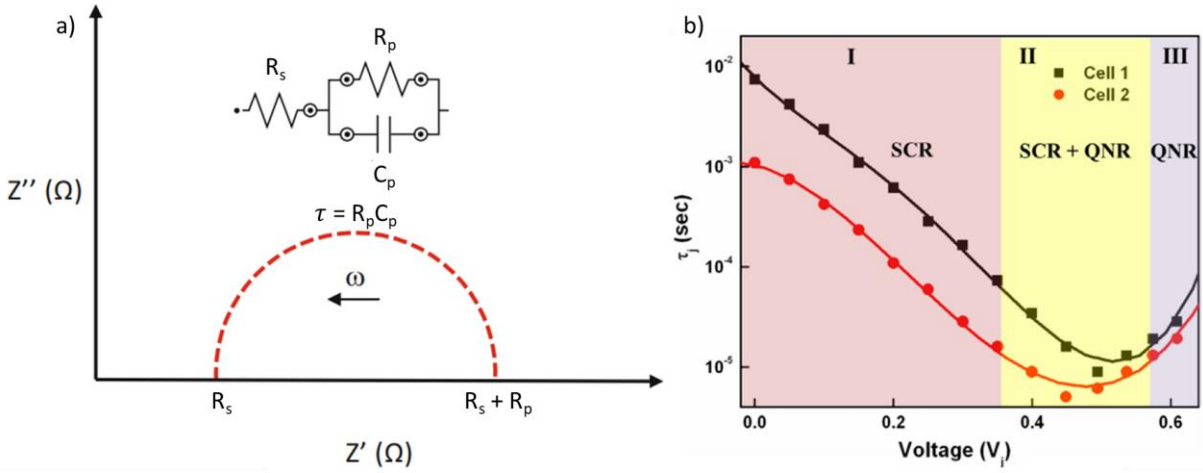

Figure 7: (a) A typical Nyquist diagram of a silicon solar cell and (b) the time constant of a polycrystalline silicon solar cell as a function of bias voltage [22], [23].

A DC bias can be applied on top of the AC signal to probe different properties of a solar cell under conditions more similar to operating conditions. For instance, in Figure 7b, the time constant of a polycrystalline solar cell is examined as a function of bias voltage. At low bias voltages, the space chare region (SCR) recombination dominates. Within a solar cell, this is occurring in the depletion layer. Increasing the forward bias, increases the involvement of the quasi-neutral region (QNR) recombination which is recombination within the p-doped region and n-doped region. Under the maximum effect of SCR and QNR recombination, the time

constant reaches a minimum where the minority carrier lifetime can be obtained. In the case of Yadav et al. (Figure 7b) both forces dominate around 0.425-0.45 V [23].

To obtain the true shunt resistance of a solar cell via impedance spectroscopy, a low positive bias or a negative bias voltage is required. The parallel resistance in the equivalent circuit (Rp) is a combination of the shunt resistance and the dynamic diode resistance (R_d) where R_d is the solar cell's ability to resist flow in the opposite direction when an AC signal is applied. Under reverse bias or low forward bias voltages, the dynamic diode resistance is larger such that the parallel resistance is equivalent to the shunt resistance [24]–[26]. At high forward bias voltages, the shunt resistance is larger such that the parallel resistance is equivalent to the dynamic diode resistance [24]–[26]. This is due to the nature of the p-n junction. A reverse bias expands the depletion layer preventing the electron-hole pairs from traveling backwards which causes R_d to dominate. A forward bias causes the depletion layer to shrink allowing free electron-hole pairs to travel in the reverse direction minimizing R_d.

Impedance spectroscopy has been primarily used in other technologies, such as dye-sensitized, organic and perovskite photovoltaics, due to the resulting impedance spectra showing multiple arcs, which each correspond to a different physical process [27]–[31]. For instance, in perovskite PV the ionic and electronic effects were decoupled to determine the ionic conductivity [32] similar to batteries [33]. With silicon PV, each process happens simultaneously, resulting in a single arc in the impedance spectra [17], such that less information is typically revealed.

2.4 Overview of Different Solar Cells

There are five groups of photovoltaics. These are multijunction (MJ) cells, single-junction gallium arsenide (GaAs) cells, crystalline silicon cells, thin-film technologies and emerging photovoltaics. Figure 8 illustrates the historical progression of all types of photovoltaics in relation to the PCE.

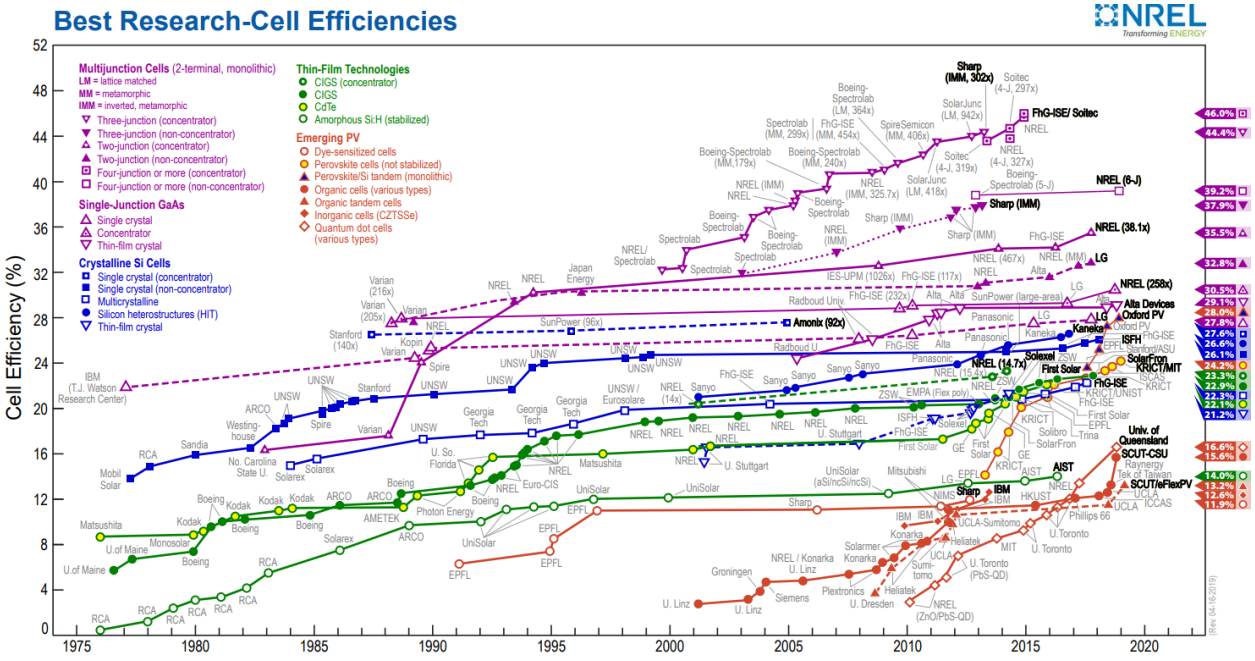

Figure 8: National Renewable Energy Laboratory (NREL) chart of highest confirmed efficiencies for photovoltaic technologies [34].

2.4.1 Crystalline Silicon Solar Cells

Crystalline silicon is the most widely adopted material for solar cell applications. Mono or poly-crystalline silicon is doped to form a p-n junction. The most efficient silicon solar cells have a PCE of 27.6% which is close to the theoretical efficiency of 33.7% [34], [35]. The limitations of this technology are the cost of manufacturing. To produce silicon, temperatures as high as 1900^{o}C are required which is only the first step of turning quartz into metallurgical-grade silicon (99% pure) [36]. Solar-grade silicon requires many steps to produce 99.9999% silicon

(~1 parts per million atoms (ppma) impurities) [36]. Examining the cost of manufacturing a module, 43% of the cost is spent on the silicon wafer [37]. Different designs have been created to improve the efficiency to cost ratio. Passivated emitter and rear contact (PERC) and bifacial solar cells employ unique architectures to enhance performance.

PERC solar cells increase the efficiency by including a dielectric passivation layer (SiN_y) at the rear of the cell as seen in Figure 9a [38]. This improves the amount of light captured near the rear surface and therefore the electron generation. The passivation layer can reflect unabsorbed light allowing a second opportunity to absorb the light while reflecting specific wavelengths that would generate heat [39]. It also reduces electron recombination at the back surface. These additions can improve the efficiency of PERC cells by up to 1% [40].

Bifacial solar cells produce power from both sides of the panel. Typical solar panels are opaque on the back-side allowing exposure from one side. Light can enter the front or back-side of a bifacial module illustrated in Figure 9b. The efficiency of this architecture is dependent on the placement and surface behind the module. A white roof would reflect more light back through the module compared to dark shingles or gravel. In ideal conditions, a bifacial module can produce up to 50% more electric power [41]. These devices are also transparent to infrared radiation which reduces the overall operating temperature [42].

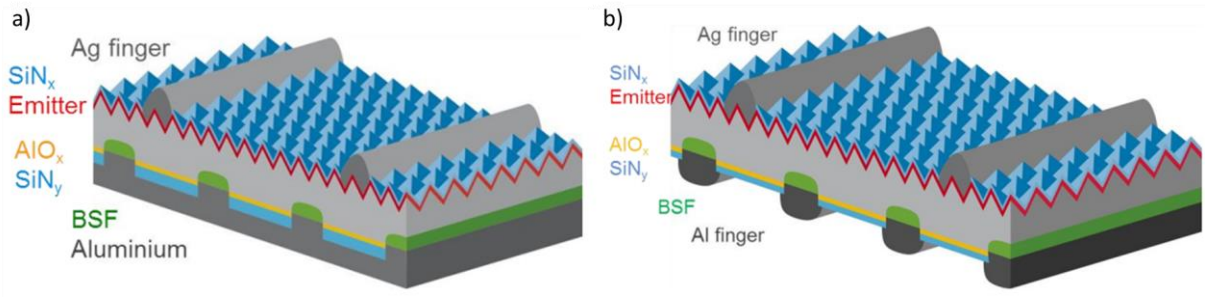

Figure 9: Schematic cross-section of (a) PERC structure and a (b) bifacial solar cell [43].

2.4.2 Multi-Junction Solar Cells

Multi-junction cells are the most efficient devices reaching efficiencies up to 46.9% [34]. In these systems, a few layers of different bandgap cells are stacked together. Buffer layers between the cells allow transport of photo-generated carriers between them [35]. Each cell absorbs a different wavelength of light. Longer wavelengths pass through the cell until they reach a layer that can absorb it. Theoretically, a multi-junction cell that can absorb the whole solar spectrum with infinite layers will have a maximum efficiency of 86.8% [44]. Due to the tedious multi-layered design, these cells are very expensive and have diminishing returns on increase of efficiency per cost of performance. The main application for these devices is when space and weight are a limiting factor such as aerospace.

2.4.3 Gallium Arsenide Solar Cells

Single junction GaAs cells have reached efficiencies of 30.5% [34]. Compared to the widely adopted silicon, GaAs has a higher electron mobility and a direct band gap making light absorption and emission more efficient. Only a few microns of GaAs are needed to absorb light compared to silicon where roughly 100 microns are needed (1 micron = 10^{-6} m). This is because of silicon's indirect band gap hindering the absorptivity of sunlight. Silicon is more abundant, is very stable and can be grown easily. There is also higher hole mobility in silicon. Since silicon is a pure element, there are no issues of stoichiometric imbalances, as in GaAs fabrication. The marginal benefits of GaAs are not yet worth the challenge of adoption over silicon technologies [45].

2.4.4 Thin-Film Technology

Thin-film technologies include copper indium gallium selenide (CIGS), cadmium telluride (CdTe), and amorphous silicon. These solar cells use layers that range from a few

nanometers (1 nanometer = 10^{-9} m) to tens of microns. This is in comparison to crystalline silicon solar cells which use wafers up to 200 μm thick. A reduction in thickness allows for flexible substrates and results in a reduction in materials used, weight, and cost. The trade-off is the efficiency being lower than in standard silicon cells and a faster rate of degradation.

2.4.5 Emerging Photovoltaics

Emerging photovoltaics include copper zinc tin sulfide (CZTS), dye-sensitized (DSSC), perovskites (PSC), organic (OSC) and quantum dot solar cells (QDSC). These technologies still require a lot of progress before commercialization but are cheaper to fabricate. CZTS solar cells have achieved efficiencies of 12.8% and have a maximum theoretical efficiency of 42% [34], [44], [46]. The current challenge is improving the efficiency by addressing the low open-circuit voltage and defects (which cause high series and low shunt resistances) [47]. DSSC, OSC and QDSC have low efficiencies and issues with long term stability [48], [49]. DSSC and QDSC also have challenges with scalability while organic solar cells are easier to manufacture [49].

Perovskite solar cells have seen a significant amount of interest emerging in 2009 with efficiencies of 3.8% and quickly rising to 24.2% in 2019 making it the fastest advancing solar technology to date [34]. Scalability and cost are addressed by consisting of cheaper materials that may be processed with printing techniques. PSCs also have a high absorption coefficient meaning a 500 nm film can absorb the complete visible spectrum. This allows for thinner, lighter and potentially flexible solar cells [48]. The challenge for these devices lies in the stability. PSCs can be damaged by elevated temperatures, humidity, light and oxygen [50].

A schematic cross section of a perovskite can be found in Figure 10a. This consists of a transparent conductive electrode (TCE), electron transport layer/material (n-type, ETL/ETM), perovskite layer, hole transport layer/material (p-type, HTL/HTM) and counter electrode. The

TCE is typically indium tin oxide (ITO) or fluorine-doped tin oxide (FTO). These layers are conductive, transparent and have a wide bandgap to not absorb or block light. The ETL and HTL are used to prevent the flow of holes/electrons to the cathode/anode respectively. The ETL/HTL also has higher charge transporting properties to move the charges that reach the ETL/HTL interface away from the perovskite layer to prevent recombination. A counter electrode, typically gold, silver or aluminum is placed on top of the cell to carry current to an external circuit. Perovskite device architectures are described as p-i-n or n-i-p where “i" is the perovskite. The n-i-p architecture (ETL/perovskite/HTL) is more common in perovskite devices than p-i-n (HTL/perovskite/ETL).

The perovskite crystal structure can be seen in Figure 10b. This is an ABX_3 structure where A, B and X are a monovalent cation (e.g, $CH_3NH_3^+$), a divalent cation (e.g, Pb^{2+}) and a monovalent anion (I^-, Br^-, or Cl^-) respectively.

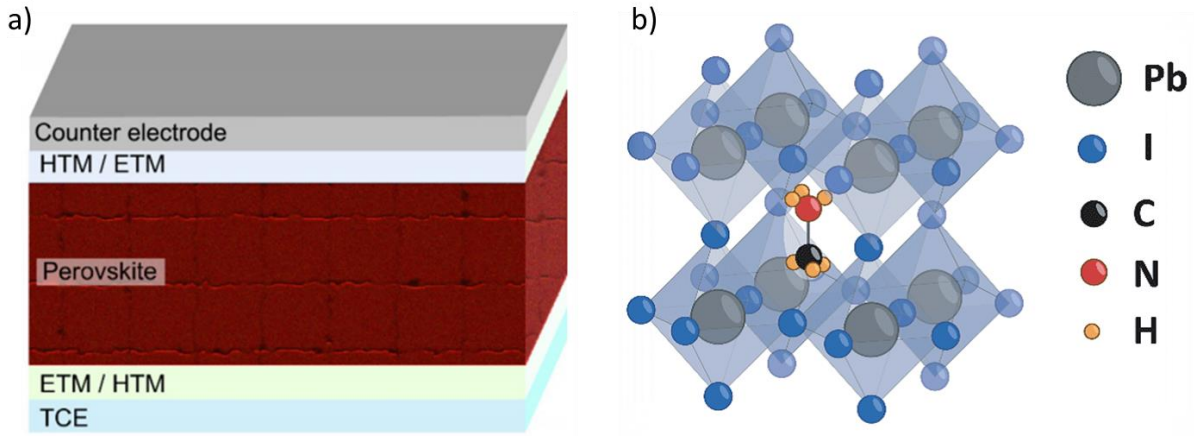

Figure 10: Schematic cross section of (a) perovskite solar cell architecture and (b) a perovskite crystal [5], [51].

2.5 Thesis Overview

This thesis aims to evaluate and address the stability of photovoltaics. Section 3.0 involves characterizing the degradation of PERC solar modules and cells by impedance spectroscopy.

Currently, specialized techniques are required to identify different types of degradation within a PERC module or cell. Impedance spectroscopy is investigated as a stand-alone technique to identify and quantify different types of degradation. Section 4.0 looks at creating a more stable architecture for perovskite solar cells using a scalable technique known as Atmospheric Pressure Spatial Atomic Layer Deposition (AP-SALD). A procedure for creating tungsten oxide (WO_3) films using this technique is developed for the first time and preliminary attempts to incorporate the WO_3 films into perovskite solar cells are discussed.

3.0 Evaluating degradation mechanisms in silicon modules by impedance spectroscopy

Passivated emitter and rear cell (PERC) and bifacial double-glass modules are commercially-important architectures for silicon photovoltaics (PV). These photovoltaics are subject to degradation mechanisms such as current-induced degradation (CID) and potential induced degradation (PID) [52]–[55], which can result in significant reductions in the power conversion efficiency (PCE) [56]. This degradation must therefore be reliably identified and addressed to ensure a suitably long lifetime for the PV modules.

Current techniques to characterize degradation include electroluminescence (EL) and photoluminescence (PL) tests, photoconductance lifetime tests, and current-voltage measurements, among others [53], [54], [56], [57]. Although the current methods are useful, individually they do not provide all information required to distinguish and quantitatively analyze degradation in a solar cell. Impedance spectroscopy is a non-destructive technique that has the potential to quantitatively analyze multiple aspects of a silicon photovoltaic's operation. Changes in the measured impedance response can be attributed to different degradation mechanisms. Impedance spectroscopy has been used to characterize corrosion of electrodes in silicon solar cells, [58] defect activation energy/concentration [59] and depletion layer defects around the p-n interface [60] in $Cu(In,Ga)Se_2$ (CIGS)-based solar cells. Notably, corrosion of the electrodes introduced another arc in the impedance spectrum, corresponding to a new time constant [58].

In this section, impedance spectroscopy is used to examine bifacial monocrystalline PERC modules in which PID was observed and standard (not bifacial) polycrystalline PERC modules and cells in which CID was observed. Comparisons between control and degraded

modules and cells are done to identify key differences and determine the extent of degradation. We find that the PID and CID examined in this study induce unique changes in the impedance spectra, making them distinguishable and quantifiable. Notably, the PID modules show a reduction in shunt resistance at low forward biases and the CID cells show a reduction in minority carrier lifetime. Different batches of cells are measured to study the effect of different processing parameters on the resulting CID, as characterized by impedance spectroscopy.

3.1 Degradation mechanisms in silicon solar cells

Potential induced degradation occurs when a module's voltage potential/leakage current causes ion mobility within a module between the semiconductor and other elements of the module (glass, antireflective coating). This causes the module's power output to decline. There are two types of PID reported in literature. Oprea *et al.* used impedance spectroscopy to study PID in c-Si PV modules in which PID caused a dramatic reduction in the measured shunt resistance [53]. Shunting-type PID (PID-s) was assumed in their case, where it is suspected that shunt paths are created by the formation of stacking faults at the SiN_x/Si interface and the migration of Na^+ ions towards the stacking faults under the influence of a high electric field [53], [61]–[63]. This is induced by an elevated temperature and a high positive bias voltage. A different PID mechanism (PID-p) has been reported for bifacial PERC modules, that has not been characterized previously with impedance spectroscopy. In PID-p, surface polarization of the cell's rear surface causes positive charges to migrate towards the AlO_x/SiN_x layer diminishing the field passivation effect of this layer. It is induced by applying a large negative bias voltage at an elevated temperature. Increasing the negative bias and or temperature accelerates PID-p [63], [64] and PID-p results in recombination along the rear surface of the module [63], [65]. A visual representation of the two PID mechanisms can be seen in Figure 11a

where PID-s effects the top part of the bifacial cell and PID-p effects the lower part of the cell. Figure 11b shows previously reported EL images of bifacial cells before and after PID has occurred. PID-s (left side of figure) shows inhomogeneous localized defects (dark streaks) in the form of stacking faults. PID-p (right side of figure) has a homogenous degradation affecting the whole back layer of the cell.

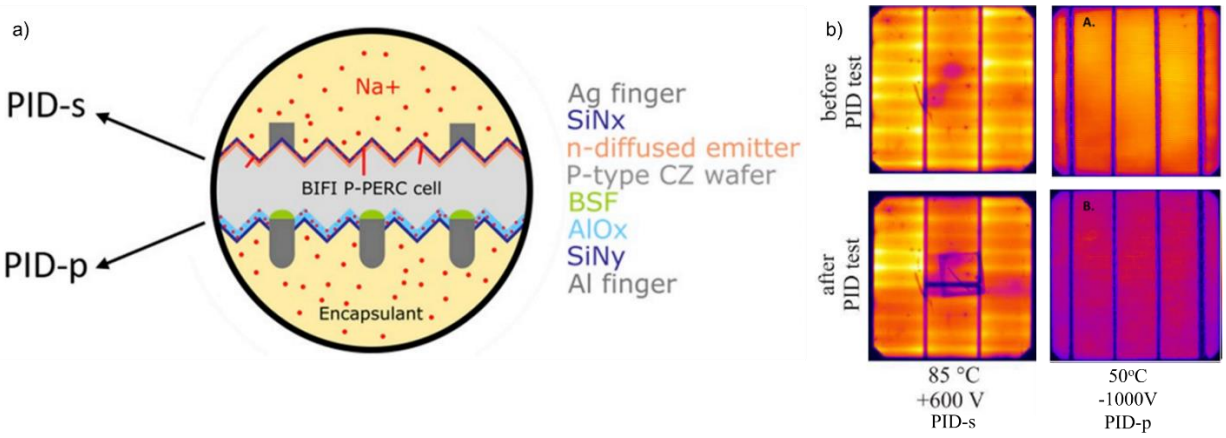

Figure 11: (a) Schematic of PID-s and PID-p degradation mechanisms on a bifacial cell with (b) corresponding EL results before and after PID. PID-s on left and PID-p on right [66]–[68]

Current induced degradation (CID) is a loss in performance arising from an initial exposure to current flowing through the cell. CID in Si solar cells or modules has not been examined by impedance spectroscopy but a reduction in minority carrier lifetimes is typically reported for CID [55], [57], which should be observable with impedance spectroscopy. CID is commonly attributed to the formation of boron-oxygen complexes in p-type silicon. Within the silicon, energy released from minority carriers during recombination activates the diffusion of oxygen, which migrates towards substitutional boron forming a metastable B-O defect. These defects act as recombination centers, which reduce the minority carrier lifetime [55], [56], [69]. Figure 12 illustrates the CID mechanism. Current and elevated temperatures stresses have been known to induce CID [52], [56], [64].

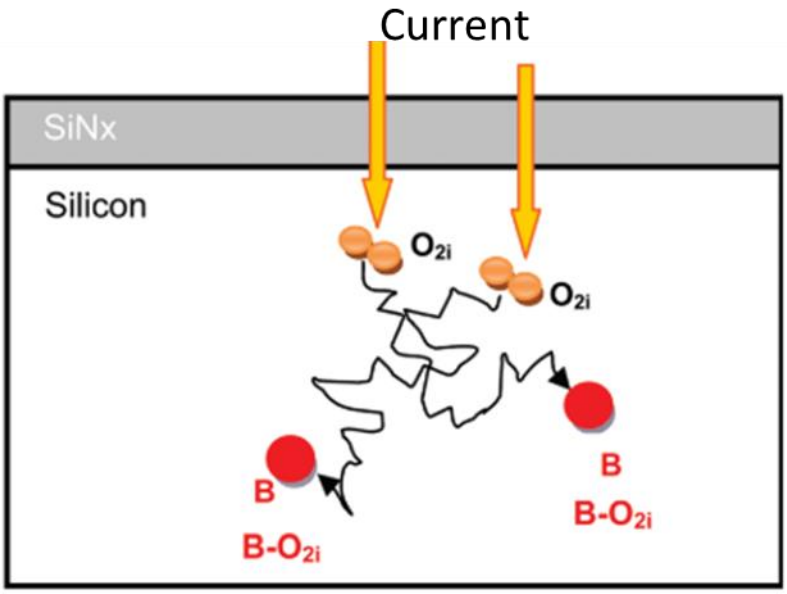

Figure 12: Schematic of CID mechanism in SiN_x solar cells. Oxygen diffuses in bulk Si to form B-O complex [70].

3.2 Experimental Conditions

3.2.1 Silicon Modules and Cells

Special PID sensitive double-glass bifacial silicon modules consisting of monocrystalline p-type passivated emitter and rear cell (PERC) cells encapsulated using Ethylene Vinyl Acetate (EVA) polymer were provided by Canadian Solar Inc. A schematic of these modules can be seen in Figure 13. Both a control module and a PID-degraded module were examined by impedance spectroscopy. The degraded module had been subjected to -1500 V at 85 °C and 85% humidity for 96 hours.

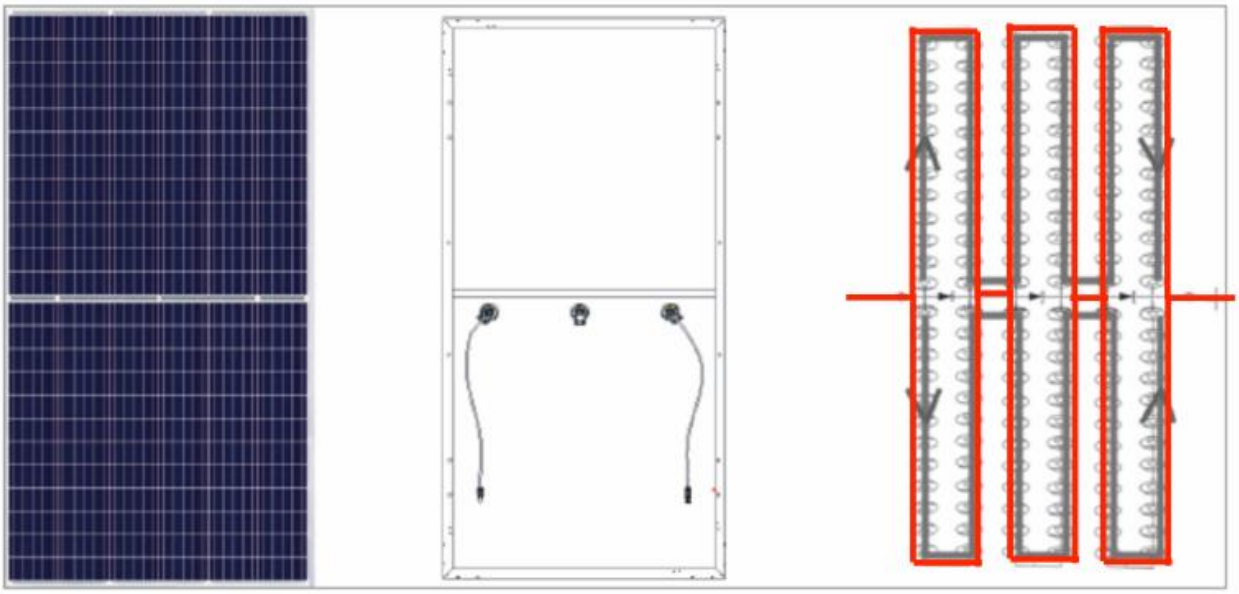

Figure 13: Schematic of PERC module with wiring shown in red. Applied bias is dropped over 72 half-cells

Standard (not bifacial) polycrystalline PERC modules were also provided by Canadian Solar Inc. A control module was again provided, along with a CID-degraded module. CID degradation had been induced by applying a current of about 0.5 A (the difference between the short circuit current, I_{SC}, and the current at maximum power, I_{MP}) at 85 °C for 200 hours.

Individual polycrystalline PERC cells were prepared by Canadian Solar Inc. using two different types of p-type silicon, which were expected to have different levels of quality. Some of the cells underwent a current induced regeneration (CIR) process prior to CID conditioning. CID was induced in half of the cells using slightly different conditioning than for the modules (3.5 A at 100 °C for 4h). A summary of the cell properties and quantity tested is provided in Table 1.

Table 1: PERC cells provided by Canadian Solar Inc.

Cell properties	Number of control cells	Number of cells after CID conditioning
High quality silicon (no CIR)	10	10
Lower quality silicon (no CIR)	15	15
High quality silicon + CIR		
Batch 1	15	15
Batch 2	10	10

3.2.2 Impedance Spectroscopy Measurements

A Gamry Interface 1000E potentiostat was used to measure the impedance of the solar modules and solar cells at room temperature. Frequencies applied were 100 kHz to 1 Hz with 10 measurements taken every decade. Above 100 kHz, the impedance of the connectors and lead wires dominate and invalidate assumptions for fitting [17], [53]. All measurements were carried out in the dark [19], [26], [54], as heating of the cells during prolonged impedance measurements and the short exposure time of standard flash testers make measurement under illumination difficult. Measurements on cells were done in a faraday cage using tungsten probe tips to contact the leads of the solar cell as seen in Figure 14 whereas modules were placed in a room with all sources of light blocked. The resulting data was analyzed using Gamry Echem Analyst. Nyquist plots were fit to an equivalent circuit with a series resistor and a resistor in parallel with a capacitor or a constant phase element. Goodness of fit was calculated by the Gamry software using the Simplex method.

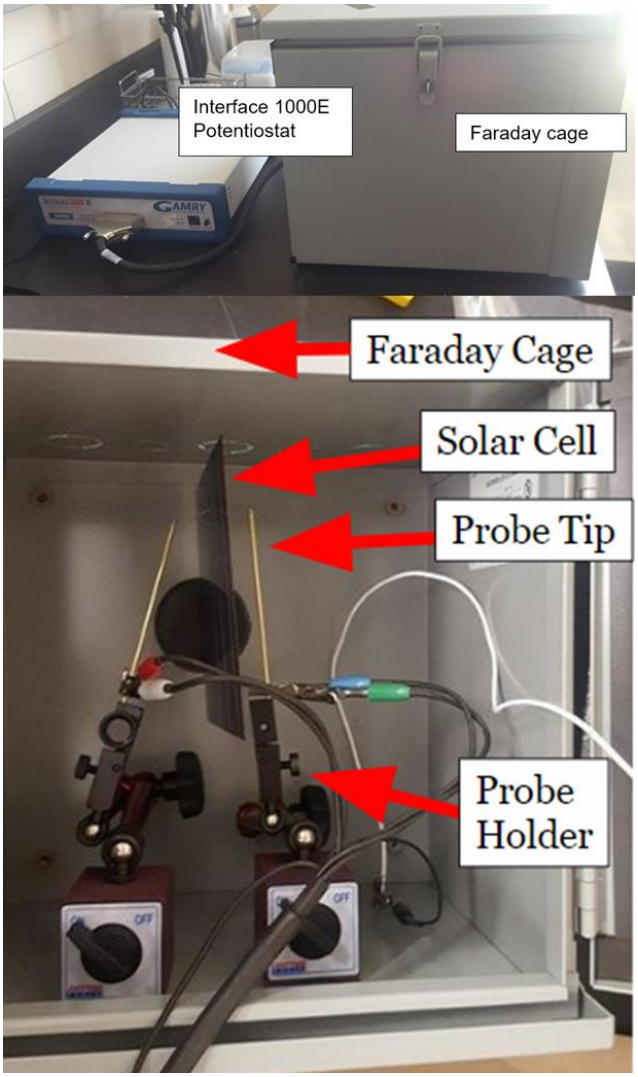

Figure 14: Impedance spectrometer and faraday cage holding a PERC solar cell. Tungsten probe tips held by magnetic articulating arms contact both leads of the cell.

3.3.3 Photovoltaic Characterization

The current-voltage curves and power conversion efficiency of the individual cells and modules were measured by Canadian Solar Inc. using a Sinton FCT-450 and a PASAN SunSim 3C (class AAA simulator), respectively. The bifacial monocrystalline PERC modules were measured by alternatively obstructing the front and rear side with a low reflectivity cover. All measurements were carried out at 1 sun, with equipment being calibrated using a standard

reference cell and a primary reference module for the cell and module measurements, respectively. BT Imaging R3 equipment was used by Canadian Solar Inc. to characterize the photoluminescence and electroluminescence of the solar cells. For EL measurements, a current of 3.5 A was used.

3.3 PID in Modules

A bifacial module was subjected to -1500 V at 85 °C and 85% humidity for 96 hours resulting in potential induced degradation. The current-voltage measurements revealed a P_{max} degradation of 37% for backside illumination and 6% for frontside illumination, where P_{max} is the maximum output power, as seen in Table 2.

Table 2: Current-voltage measurements of a (one) bifacial module before and after PID conditioning with simulated solar illumination on the front or backside.

State	V_{OC} (V)	I_{SC} (A)	V_{MP} (V)	I_{MP} (A)	Fill Factor	P_{MAX} (W)	% Decrease P_{MAX}
Front							
Initial	47.548	9.618	39.450	9.101	0.785	359.038	
After PID	46.646	9.400	38.575	8.740	0.769	337.148	6.1
Back							
Initial	46.893	7.102	39.477	6.782	0.804	267.716	
After PID	45.785	6.451	40.992	4.104	0.570	168.222	37.2

Figure 15a shows the Nyquist plots for the double-glass monocrystalline bifacial silicon modules with and without PID that were measured with a DC bias of 5 V applied across the 72 cells in series, resulting in a bias of approximately 0.07 V per cell. AC voltages of 100 mV and 400 mV were applied and were found to result in identical spectra, as shown in Figure 15a. A reduction in the parallel resistance (width of the semicircle in the Nyquist plot) of more than 1 order of magnitude is observed for the PID-degraded module. The parallel resistance is a parallel combination of the dynamic diode and shunt resistances. Under increasing forward bias, the

dynamic diode resistance is known to decrease to negligible values [24]–[26], such that the parallel resistance is equivalent to the dynamic diode resistance. When the bias voltage is close to zero or reverse biased, the diode resistance is expected to be much greater than the shunt resistance, making the parallel resistance equivalent to the shunt resistance [25]. Ideally a reverse bias would be applied to the modules to isolate the shunt resistances, but this was not possible due to reverse-polarity-protection, which prevents reverse voltages from damaging the circuit [71], [72]. Instead, the DC voltage was kept low to limit the impact of the dynamic diode resistance, such that the measured parallel resistance should approximate the shunt resistance. A plot of Rp versus bias voltage for some of the individual PERC cells is included in Figure 16 and shows that the parallel resistance only started to decrease significantly (indicating the influence of the dynamic diode resistance) when the cell voltage was greater than 0.1 V. Hence, at a 5 V bias (0.07 V per cell), the parallel resistance is expected to closely approximate the shunt resistance.

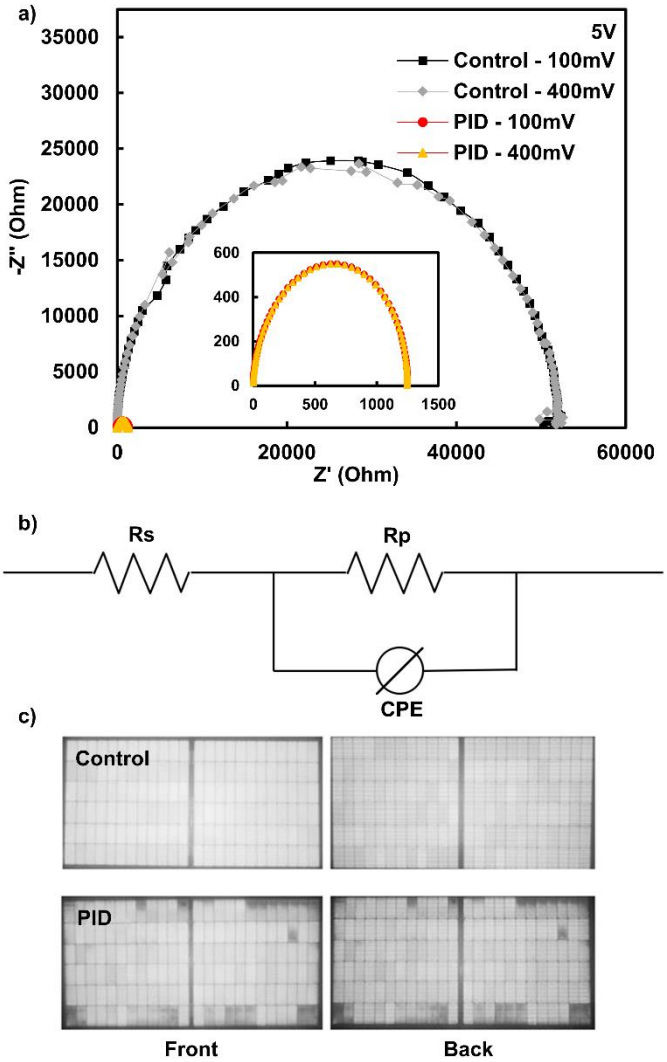

Figure 15: Characterization of bifacial modules with and without PID. (a) Nyquist plots of the bifacial modules measured at a 5 V bias using 100 mV and 400 mV AC voltages. (b) Equivalent circuit used to fit the Nyquist plots. (c) Electroluminescence measurements of the control and PID-degraded modules from the front and back.

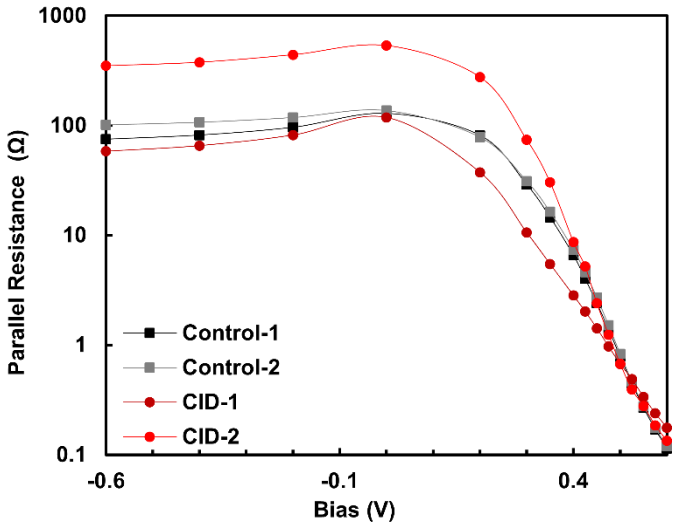

Figure 16: Parallel resistance as a function of bias voltage for 4 high quality silicon PERC cells (with no CIR). Two of the cells underwent CID conditioning and two did not. The parallel resistance was obtained by fitting the impedance spectra to an equivalent circuit with a series resistor, parallel resistor, and parallel capacitor.

The Nyquist plots were fit to an equivalent circuit with a constant phase element (CPE), as shown in Figure 15b, which provided a better fit than a circuit with a simple capacitor. A constant phase element is typically used when the Nyquist plot deviates from a perfect semicircle due to inhomogeneity in the circuit and is associated with traps and defects [73]–[75]. The elements of a CPE include Q and ϕ, as given in Equation 3.

$$Z = \frac{1}{(Q\omega i)^{\phi}} \quad (3)$$

ϕ is a value between 0 and 1, where 1 corresponds to the element being an ideal capacitor and 0 being a resistor. Q is the capacitance when $\phi \approx 1$. Table 3 lists the equivalent circuit parameters obtained for the bifacial modules at the two AC voltages. The fitted parallel resistance R_p, drops significantly from approximately 51 kΩ in the control module to 1.2 kΩ in the module with PID, consistent with the Nyquist plot in Figure 15a. The series resistance remains very small, suggesting that significant contact degradation does not occur [17], [58], [76]. It is seen that ϕ is

0.996 for the control module and 0.960 for the PID module. This indicates uniformity within a cell and from cell-to-cell in the circuit for the control module and slight inhomogeneity for the PID module. Since ϕ>0.95 the spatial inhomogeneity can be considered relatively small [77]. The inhomogeneity is confirmed in EL test results seen in Figure 15c where the cells in the PID-degraded module show more darkening, particularly around the edges of the module. However, within the cells there does not appear to be significant localized areas of darkening. Hence the decrease in ϕ can be attributed to a non-uniform degradation across the module, where the cells along the edges experience greater PID.

Table 3: Equivalent circuit parameters for one bifacial module with PID and one without PID (at 5V bias)

	R_s (Ω)	R_p (Ω)	Q (F)	ϕ	Goodness of Fit
Bifacial Control 100mV	1.16E-07	5.15E+04	1.37E-07	0.996	3.12E-03
Bifacial Control 400mV	2.66E-06	5.06E+04	1.38E-07	0.996	3.93E-03
Bifacial PID 100mV	1.07E-06	1.24E+03	2.13E-07	0.960	2.30E-03
Bifacial PID 400mV	1.07E-06	1.24E+03	2.13E-07	0.960	2.30E-03

Overall, there is a P_{max} loss of approximately 37% for backside illumination (Table 2) and a loss in shunt resistance of more than 1 order of magnitude (as measured by impedance spectroscopy) in the PID-degraded bifacial module. Oprea *et al.* previously reported a larger P_{max} loss of approximately 70% for crystalline-silicon (c-Si) modules experiencing PID and similarly observed a larger drop in shunt resistance of 3 orders of magnitude by impedance spectroscopy (measured using a 2 V bias and 2 V AC signal) [53]. It is noted that in the modules measured by

Oprea *et al.*, the P_{max} loss was mainly due to a reduced fill factor and open-circuit voltage. They attributed the PID to Na^+ diffusion into stacking faults (PID-s). Although they used a simple capacitor in the equivalent circuit, PID-s defects are expected to result in significant inhomogeneity due to localized shunt pathways in the cell [65], [67], such that a constant phase element may have been more suitable (goodness of fits were not provided in their paper). In the PID-degraded module measured here, the P_{max} loss was mainly due to a reduced fill factor and short circuit current (current-voltage measurements are included in Table 2 and Figure 17), consistent with PID caused by a deterioration of the field passivation effect (PID-p). It has been reported that the cell fill factor is only moderately affected by PID-p, whereas the module fill factor decreases significantly due to PID-p, which was attributed to mismatch between the various degraded cells in the module [65], [68]. PID-p has been reported to produce homogenous cell degradation related to increased surface recombination [63], [65], [67]. This is consistent with the lack of localized defects observed within the cells in the EL measurements in Figure 15c, and the modest deviation of the CPE parameter ϕ from 0.996 to 0.960 in the module's equivalent circuit. Thus, impedance spectroscopy may not only allow identification and quantification of PID via a reduction in the shunt resistance but may also permit different modes of PID to be distinguished (e.g., an equivalent circuit with a CPE may show a distinction between PID-s and PID-p in modules based on the CPE parameters). Study of modules with a wider variety of PID conditions can be pursued in the future to confirm this.

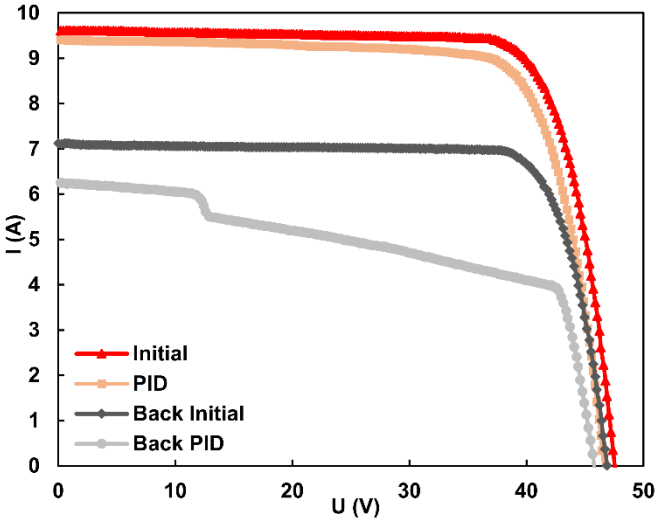

Figure 17: Current-voltage measurements of bifacial modules with and without PID, demonstrating a reduction in fill factor and short circuit current, particularly for backside illumination.

3.4 CID

3.4.1 CID in Modules

A PERC module was subject to a current of about 0.5 at 85 °C for 200 hours resulting in current induced degradation. The current-voltage measurements revealed a P_{max} degradation of ~2%, as seen in Table 4.

Table 4: Current-voltage measurements of a (one) PERC module under simulated solar illumination before and after CID conditioning

State	V_{OC} (V)	I_{SC} (A)	V_{MP} (V)	I_{MP} (A)	Fill Factor	P_{MAX} (W)	% Decrease P_{MAX}
Initial	39.192	9.602	32.616	9.105	0.789	296.958	
After CID	39.138	9.519	32.443	9.004	0.784	292.120	1.6

Figure 18a shows the Nyquist plots for the polycrystalline PERC modules with and without CID, again at a DC bias of 5 V. As before, similar results were obtained using 100 mV and 400 mV AC voltages. In contrast to the PID-degraded monocrystalline bifacial module, in which a large reduction in shunt resistance was observed, a slight increase in shunt resistance is

observed for the CID-degraded PERC module. This is unexpected as the shunt resistance is expected to decrease under CID [64], [78]. However, the shunt resistance only increases by approximately 12%, as compared to the more than an order of magnitude reduction in shunt resistance observed in the PID module, such that this increase in R_p is attributed to variability amongst the cells and modules, rather than the current-induced degradation. Figure 16 supports this, where it is seen that at bias voltages near zero, the R_p of individual control and CID polycrystalline PERC cells varies, with some CID cells having a larger R_p than the control cells. As the bias voltage increases, the R_p dips to expected values and is lower in the CID cells than the control cells. Others have similarly reported that due to the sensitive nature of impedance spectroscopy, a significant impedance variability can be found within batches of modules and cells [64], [79]–[81].

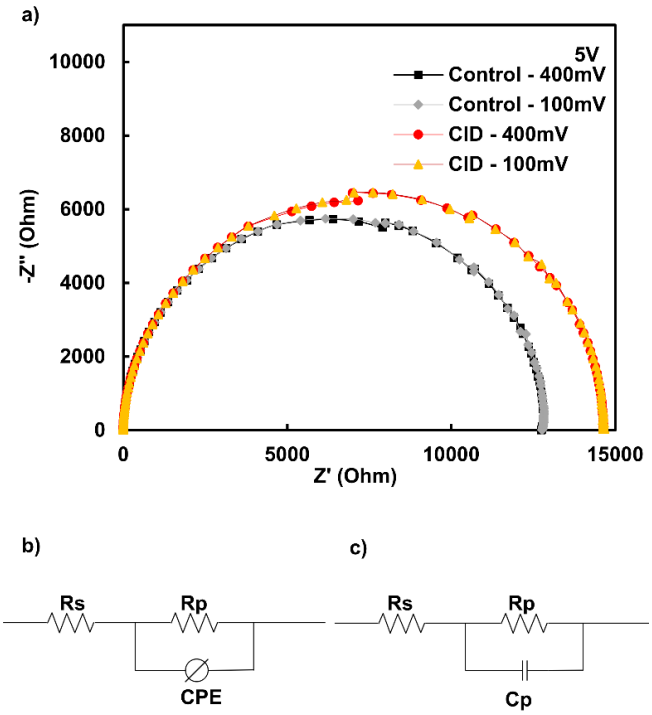

Figure 18: Characterization of PERC modules with and without CID. (a) Nyquist plots of PERC modules measured at a 5 V bias using 100 mV and 400 mV AC voltages. (b-c) Equivalent circuits used to fit the Nyquist plots with a constant phase element and a capacitor respectively.

The Nyquist plots were again fit to a circuit with a constant phase element, as shown in Figure 18b, and the obtained equivalent circuit parameters are found in Table 5. As for the case of PID in the bifacial modules discussed in Section 3.3, an increase in the series resistance was not observed for CID in the standard PERC modules. Unlike for the bifacial modules, it is seen in Table 5 that ϕ is very close to 1 for both PERC modules (with and without CID). Hence the PERC modules can be accurately fit to an equivalent circuit with a capacitor instead of a constant phase element, as shown in

Figure 18c and Table 5. Fitting to a capacitor C_p facilitates the analysis of CID because a reduction in minority carrier lifetime is expected for CID, which can be measured by examining the time constant of the Nyquist plot [55], [57]. As indicated in the lower portion of Table 5, the module-level time constants obtained for the CID-degraded module in

Figure 18 were actually slightly larger than those obtained for the control module. Since these measurements were performed at a 5 V forward bias, a bias of only approximately 0.07 V was applied to each of the 72 cells in series. The minority carrier lifetime in the PERC cells cannot be accurately measured at this bias. Higher bias voltages of about 0.5 V per cell are required. In this bias range, the space charge region (SCR) recombination and quasi-neutral region (QNR) recombination are both present and the combined influence of both mechanisms on the carrier lifetime is maximized [23]. Therefore, it was identified that to accurately identify CID in silicon modules, an impedance spectrometer capable of applying larger bias voltages (e.g., greater than 40 V) would be required for further investigation. It is noted that while common impedance spectrometers are not capable of such high bias voltages, some manufacturers do produce models that can produce biases in this range.

Table 5: Equivalent circuit parameters for one PERC module with CID and one without CID obtained by fitting equivalent circuits with a CPE or a capacitor (at 5 V bias)

CPE	**Rs (Ω)**	**Rp (Ω)**	***Q* (F)**	***Φ***	**Goodness of Fit**
PERC Control 100mV	6.15E-06	1.26E+04	1.68E-07	0.992	2.28E-03
PERC Control 400mV	2.11E-06	1.26E+04	1.67E-07	0.993	2.28E-03
PERC CID 100mV	1.01E-01	1.43E+04	2.02E-07	0.988	4.09E-03
PERC CID 400mV	1.27E-01	1.43E+04	1.99E-07	0.989	4.16E-03
Capacitor	**Rs (Ω)**	**Rp (Ω)**	**Cp (F)**	**Time Const. (s)**	**Goodness of Fit**
PERC Control 100mV	3.77E-01	1.26E+04	1.56E-07	1.95E-03	2.45E-03
PERC Control 400mV	1.28E-03	1.26E+04	1.55E-07	1.95E-03	2.48E-03
PERC CID 100mV	3.93E-01	1.42E+04	1.80E-07	2.56E-03	4.64E-03
PERC CID 400mV	5.97E-07	1.42E+04	1.79E-07	2.55E-03	4.70E-03

3.4.2 CID in Cells

To assess the ability of impedance spectroscopy to identify and quantify CID, polycrystalline PERC cells were studied, as a suitably large bias voltage could be applied with the standard spectrometer used. The cells that were made from high quality silicon and did not undergo current induced regeneration (CIR) were measured at bias voltages ranging from -0.4 V to 0.6 V using an AC voltage of 10 mV. The resulting Nyquist plots were fit well using an equivalent circuit consisting of a series resistor, parallel resistor, and parallel capacitor. The time constants obtained from the equivalent circuits were plotted as a function of bias voltage, as

shown in Figure 19. At lower bias voltages, the time constant is relatively constant. The space charge region (SCR) recombination dominates at low forward and reverse biases (-0.4 to 0.35V). As the forward bias increases, the involvement of shunt resistance increases causing the time constant to decline. The bias voltage increases to a zone where the SCR and quasi-neutral region (QNR) recombination are both present causing the time constant to further decrease (0.35 to 0.55V) [23]. Under the maximum effect of SCR and QNR recombination, the time constant reaches a minimum where the minority carrier lifetime can be obtained [23]. This is seen to occur at a bias voltage of approximately 0.5 V in Figure 19 and can vary from cell to cell. Thus, minority carrier lifetimes of 29 μs and 42 μs are obtained from Figure 19 for the cells with and without CID, respectively.

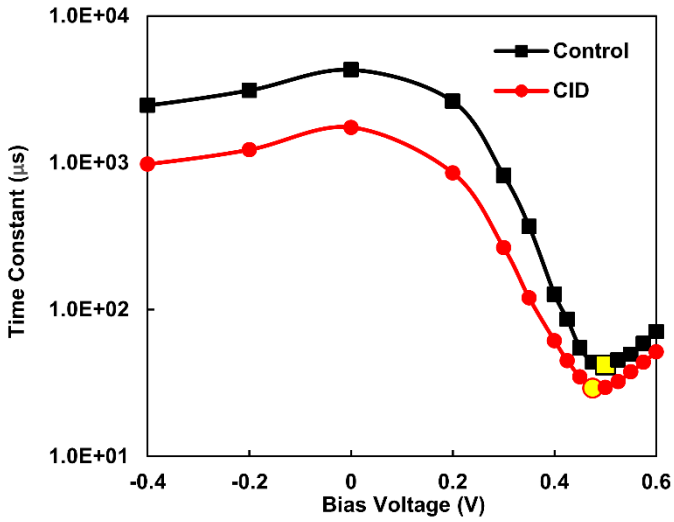

Figure 19: Time constant as a function of bias voltage for high quality silicon PERC cells (with no CIR), with and without CID conditioning.

The minority carrier lifetimes of all 100 PERC cells were measured in a similar manner, and a clear relationship was observed with the measured PCEs. In Figure 20, the lifetimes of the batches of cells with varying pre-treatments are shown as a function of their PCE. These plots clearly illustrate the effects of CID. CID cells are clustered in the bottom left of the plots,

corresponding to lower PCE and minority carrier lifetime values, whereas the cells that did not undergo CID conditioning are located in the upper right, with higher PCEs and lifetimes. This suggests that impedance spectroscopy can provide a quantitative measure of the degree of CID (in terms of the reduction in minority carrier lifetime) within a batch of solar cells.

To compare the effectiveness of the different CID mitigation strategies (high quality silicon and CIR), the percent reductions in average PCEs and minority carrier lifetimes resulting from CID conditioning are compared for different cell batches in Table 6. The percent decreases in average minority carrier lifetimes and average PCEs resulting from CID conditioning were large for batches where CIR was not employed. That is, 16.72% and 19.26% decreases in average lifetime and 1.62% and 1.78% decreases in average PCE were observed for the lower quality Si (no CIR) and high-quality silicon (no CIR) batches, respectively. It should be noted that the decreases were smaller than expected in batches where the silicon was expected to be of lower quality. This suggests that the quality may not be inferior, or this silicon is less susceptible to CID. The smallest percent decreases are observed in batch 1 of the cells that used high quality silicon and CIR. This batch demonstrated a 12.21% decrease in average minority carrier lifetime and a 1.35% decrease in PCE. These results suggest that CIR is an effective process in reducing CID in the polycrystalline PERC cells.

Interestingly, the other high-quality silicon and CIR batch (batch 2) showed a larger decrease in average minority carrier lifetime (18.53%) but a similar decrease in average PCE (1.34%) when compared to batch 1. This indicates that while a relation between PCE and minority carrier lifetime can be observed within a batch of cells (as shown in Figure 20), the relationship between % reduction in average PCE and % reduction in lifetime resulting from CID may vary from batch to batch. This is likely due to parameters other than those considered here

(type of silicon, use of CIR treatment) influencing the cells' response to CID conditioning [64], [79]–[81].

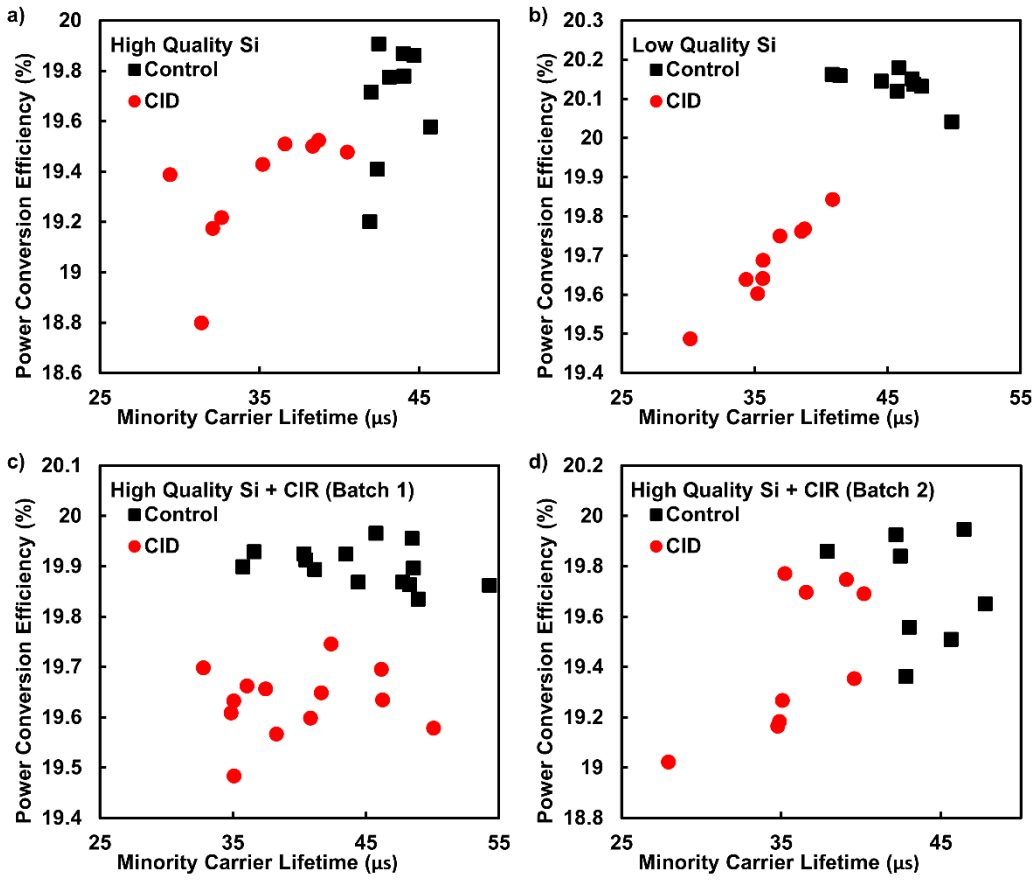

Figure 20: Minority carrier lifetime as a function of power conversion efficiency for batches of varying pre-treatments: (a) high quality Si (no CIR), (b) lower quality Si (no CIR), (c) high quality Si + CIR (batch 1), (d) high quality Si + CIR (batch 2).

Table 6: Lifetime and PCEs of PERC cells with and without CID conditioning

Cell Properties	**Number of Cells**	**CID Conditioning**	**Lifetime (μs)**	**% Decrease Lifetime due to CID**	**PCE (%)**	**% Decrease PCE due to CID**
High quality Si (no CIR)	10	No	43.3 ± 1.4		19.68±0.01	
High quality Si (no CIR)	10	Yes	35.0 ± 1.3	19.26%	19.33±0.08	1.78%
Lower quality Si (no CIR)	15	No	43.0 ± 1.7		19.98±0.02	
Lower quality Si (no CIR)	15	Yes	35.8 ± 0.9	16.72%	19.68±0.03	1.62%
High quality Si + CIR (Batch 1)	15	No	45.3 ± 1.5		19.90±0.01	
High quality Si + CIR (Batch 1)	15	Yes	39.8 ± 1.5	12.21%	19.63±0.02	1.35%
High quality Si + CIR (Batch 2)	10	No	44.1 ± 1.1		19.69±0.01	
High quality Si + CIR (Batch 2)	10	Yes	35.9 ± 1.2	18.53%	19.43±0.09	1.34%

3.5 Conclusions

Impedance spectroscopy is a powerful tool with capabilities yet to be fully exploited in the field of silicon photovoltaics. Here it was used to distinguish and quantify PID-p and CID in silicon solar modules and cells. PID-p in double glass bifacial modules was characterized by a dramatic reduction in shunt resistance. Comparison to a previous report on PID-s indicates that larger reductions in shunt resistance correspond to more degradation. While other techniques, such as IV measurements, can be used to measure the shunt resistance, by fitting the impedance spectroscopy data to an equivalent circuit with a constant phase element, this technique also

provides a measure of the degree of inhomogeneity within the module (as indicated by the constant phase element parameter ϕ), which has the potential to distinguish between PID-p and PID-s.

CID was characterized by examining the minority carrier lifetime of cells due to the high bias voltages required to probe the minority carrier lifetime in a module. A correlation between PCE and minority carrier lifetime was observed, with a lower lifetime due to CID resulting in a lower PCE. CID did not affect the shunt resistance significantly, such that CID and PID are distinguishable by impedance spectroscopy. The influence of different silicon wafers and a current-induced regeneration process on the extent of CID in the PERC cells was characterized. While the CIR process was found to reduce the amount of CID, the use of what was expected to be lower quality silicon wafers did not lead to a clear reduction in the minority carrier lifetimes.

Overall, impedance spectroscopy appears to be a promising method for characterising degradation mechanisms in solar cell modules. In particular, it is well suited for non-destructive measurements in the field and in factory settings. To further clarify its abilities, the methodology demonstrated here can be applied to solar cells and modules displaying a wider variety of degradation mechanisms of varying degrees in the future.

4.0 Creating Tungsten Oxide by AP-SALD for Next Generation Perovskite Solar Cells

Emerging photovoltaics such as perovskite solar cells are of extreme interest when tackling the global energy problem. To make renewable energy more enticing, the cost must be reduced while efficiencies increase. Perovskites are an efficient, economically feasible, scalable device.

Currently, the issue in perovskites is the long-term stability. Degradation caused by temperature, light and humidity is impeding commercialization [82]. During fabrication, humidity enhances perovskite crystal formation resulting in higher quality, carrier mobility and lifetime [83]. However, excess moisture is known to damage the crystallinity once films are prepared [50], [83]. Because this is very difficult to control, nearly all groups are known to fabricate perovskites in a dry atmosphere [50], [82]. New materials and architectures must be designed to overcome these problems.

Metal oxide transport layers are versatile and stable compared to the organic and carbon-based materials commonly used in PSCs [29], [82], [84]. To create an efficient transport layer, the energy levels must match the perovskite. For instance, the work function of the electron transport material must align with the conduction band (CB) of the perovskite. Likewise, the hole transport material must align with the valence band (VB). The energy levels of suitable materials that may construct a device can be seen in Figure 21. The transport layers must also form a good interface with the perovskite film for nucleation and crystal growth to ensure efficient transfer of electrons and holes and be relatively transparent to allow the perovskite to absorb as much light as possible [85]. Tungsten oxide has a bandgap between 2.6 to 3.0 eV with VB energy levels around -5.5 eV [86], [87]. The conductivity is comparable to NiO_x and it is chemically stable,

environmentally friendly and insoluble to water making it attractive for a hole transport material [87], [88].

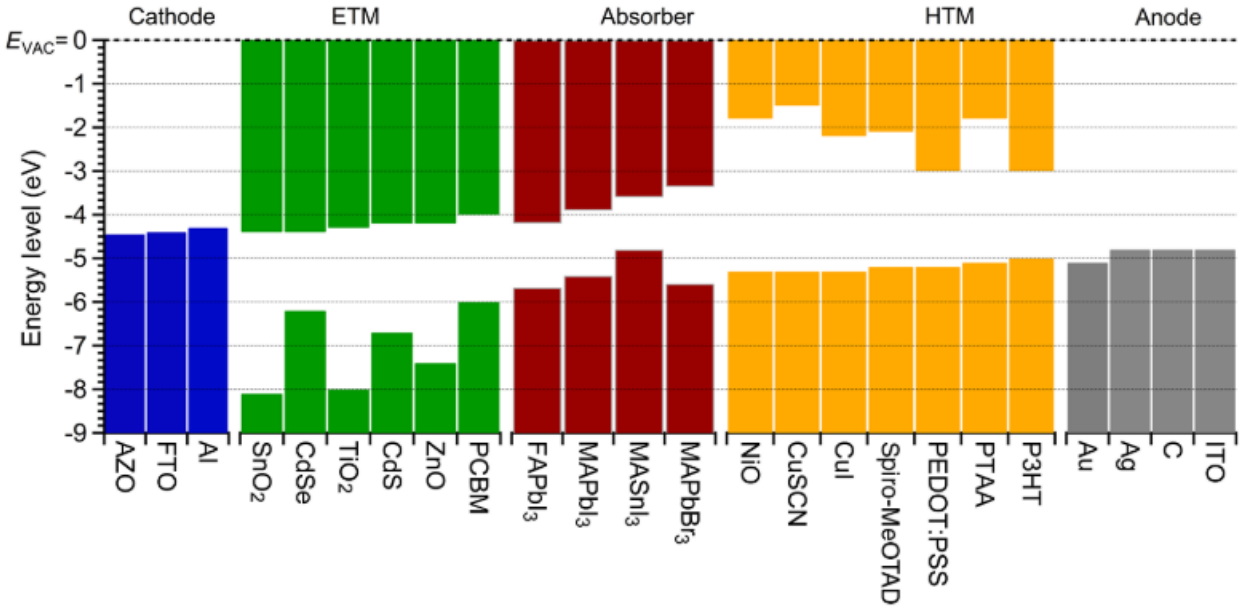

Figure 21: Energy levels, for cathode (blue), electron transport material (green), absorber/perovskite (red), hole transport material (yellow) and anode (gray) [89].

In this section, WO_3 films will be deposited using a scalable atmospheric pressure spatial atomic layer deposition (AP-SALD) technique for the first time. This is enabled by the incorporation of a nebulizer and ozone generator into an existing, custom-built AP-SALD system. The resulting WO_3 films are characterized, and their incorporation into PSCs is discussed.

4.1 Tungsten Oxide in Perovskite Solar Cells

There is not a lot of literature available for tungsten oxide in perovskites compared to other metal oxides. Tungsten oxide is commonly used in mesoscopic n-i-p structures as an additive to an ETL in the form of nanoparticles or nanocrystals [90]–[92]. The WO_3 is commonly spin coated. Mahmood et al. electro sprayed WO_3-TiO_2 core-shell nanocrystals as an

ETL to create FTO/WO_3/TiO_2/Perovskite/Spiro-OMeTAD/Au devices of 11.24% efficiency [92]. Kim et al. spin coated WO_3 in addition to Spiro-OMeTAD to create an inorganic-organic double layered HTL. This layer prevents the evaporated metal electrode from permeating into the perovskite while promoting the formation of uniform pin-hole free Spiro-OMeTAD. This enhances the thermal and moisture resistance of the PSC. The device architecture was FTO/SnO_2/Perovskite/WO_3/Spiro-OMeTAD/Au and produced an efficiency of 21.44% [87]. Conversely, Kianoosh et al. used WO_3 on top of the Spiro-OMeTAD layer in FTO/PEDOT:PSS/perovskite/Spiro-OMeTAD/WO_3/Au devices showing a similar improvement in device stability [93].

There have also been a few attempts at using tungsten oxide in inverted p-i-n devices. Some groups fabricated monoclinic tungsten oxide nanocrystals as a hole transport layer using spin coating methods [88], [90]. Sofia et al. achieved efficiencies of 13.3% which is the highest reported for perovskites using an unmodified crystalline WO_3 as the interlayer [88]. The architecture is demonstrated in Figure 22. The thickness of the WO_3 HTL was optimized at 40 nm.

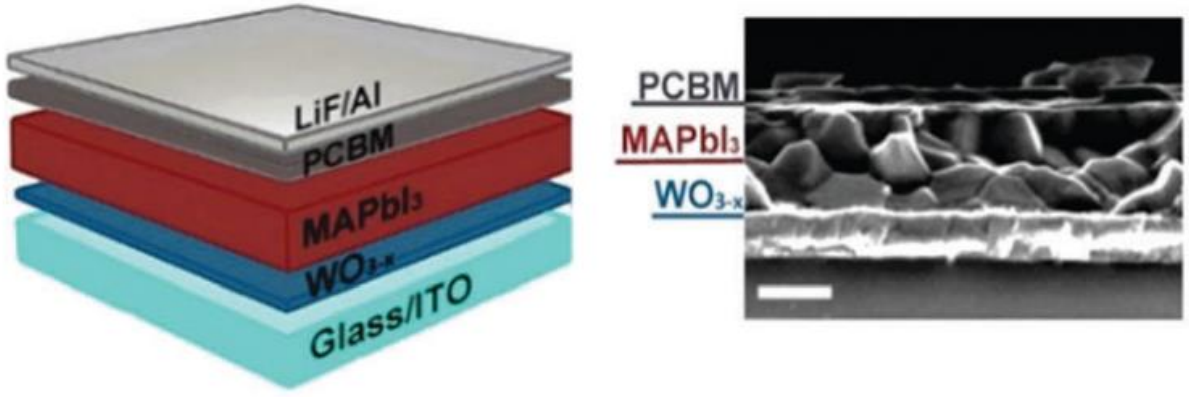

Figure 22: Inverted p-i-n devices using unmodified WO_3 nanocrystals as a hole transport layer. Including sketch of sandwich device and SEM cross section of device at a scale of 300 nm [88].

4.2 Atmospheric Pressure Spatial Atomic Layer Deposition

The method of manufacturing directly affects the performance and stability of a PSC. Spin coating and vacuum thermal evaporation are the popular methods for depositing inorganic hole transport materials [94]. These methods generally produce uniform films. Figure 23 shows different methods for fabricating thin film hole transport materials for use in perovskite solar cells in relation to the PCE. Dip coating, screen printing, vacuum deposition, electro deposition, pulsed laser deposition, combustion and spray pyrolysis deposition all show promise when producing metal oxide thin films.

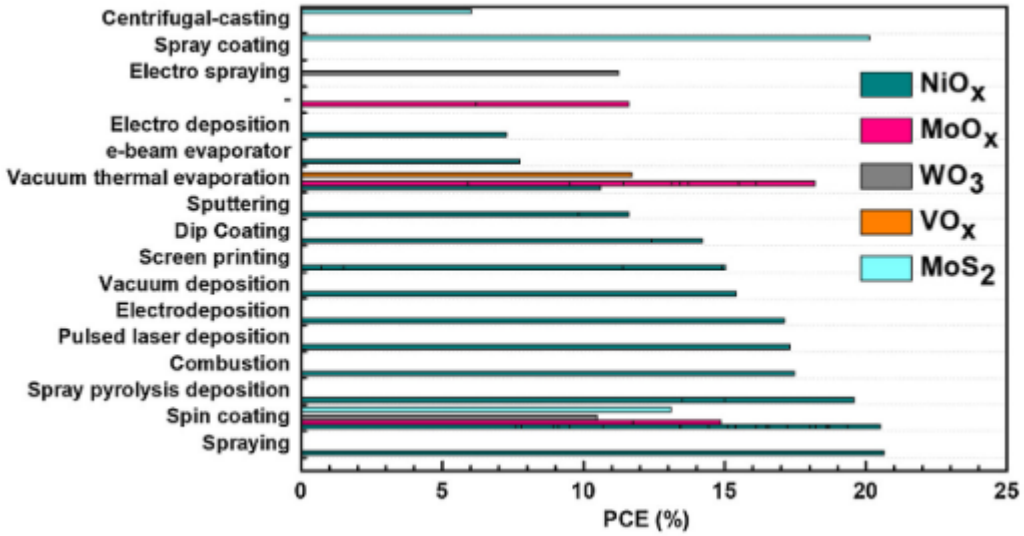

Figure 23: Different methods used for synthesizing thin film hole transport materials for perovskite solar cells in relation to PCE [94].

In terms of commercialization, a scalable technique that can produce high quality films is desired. There has been a rising interest in atomic layer deposition as a technique to generate higher-quality, dense, pinhole free films. ALD operates by the sequential repetition of self-limiting surface reactions. By sequentially filling a chamber with a precursor (precursor A) which absorbs a single layer on a heated substrate, venting, then adding a second precursor

(precursor B) which reacts with the previously deposited layer of precursor A, a film is grown at an atomic scale. A schematic of this process is seen in Figure 24 where a single ALD cycle is used to grow a monolayer of aluminum oxide. This cycle can be repeated multiple times, to build up a thin film one atomic layer at a time. This allows tunability of the optical, chemical and electronic properties of the films by changing the film density, stoichiometry and doping levels. Importantly, high-density, pinhole free films are produced that can prevent the ingress of water and improve charge transport properties. These are keys to the stability of a perovskite solar cell.

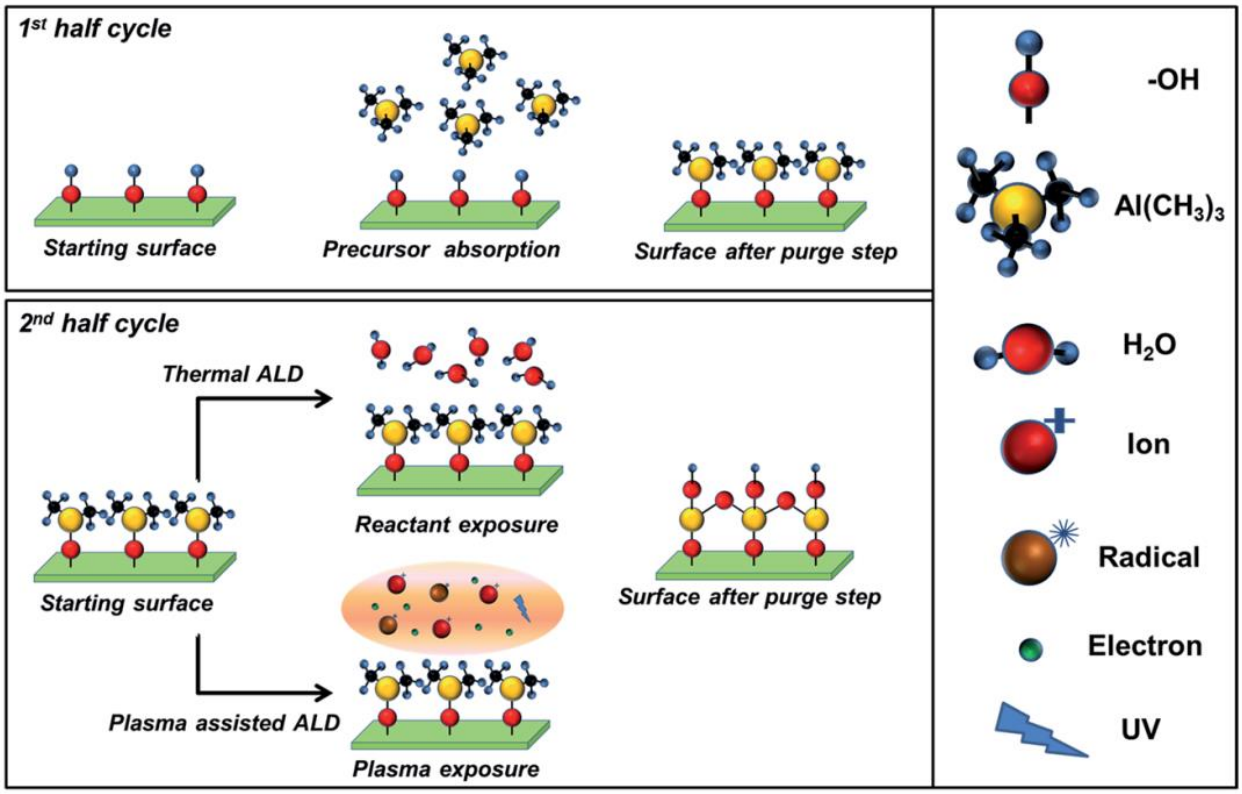

Figure 24: Schematic of one ALD cycle for Al_2O_3. Precursor A is tri-methyl-aluminum and precursor B is water in the thermal ALD case, and O_2 plasma in the plasma assisted ALD case.

Traditional atomic layer deposition suffers from low-throughput and high production costs. This is a vacuum based process which requires precursors to be vented and purged after

each step. Growing films is a lengthy process with excess precursor being wasted at each stage. AP-SALD overcomes these issues and offers a high-throughput solution as seen in Figure 25. Rather than separate the precursors in time by sequentially purging, the precursors are confined to separate regions. An oscillating stage moves the substrate into regions containing the two precursors. After passing between both regions, an ALD cycle is completed. The ALD cycle time is no longer limited by the time to fill and purge the deposition chamber. Instead it is limited only by how fast a substrate can travel between the two precursor zones. The essence of ALD is sequentially exposing a substrate to different precursors without intermixing. Conventional ALD requires vacuum chamber purge steps while spatial ALD uses physical barriers or gas curtains [95].

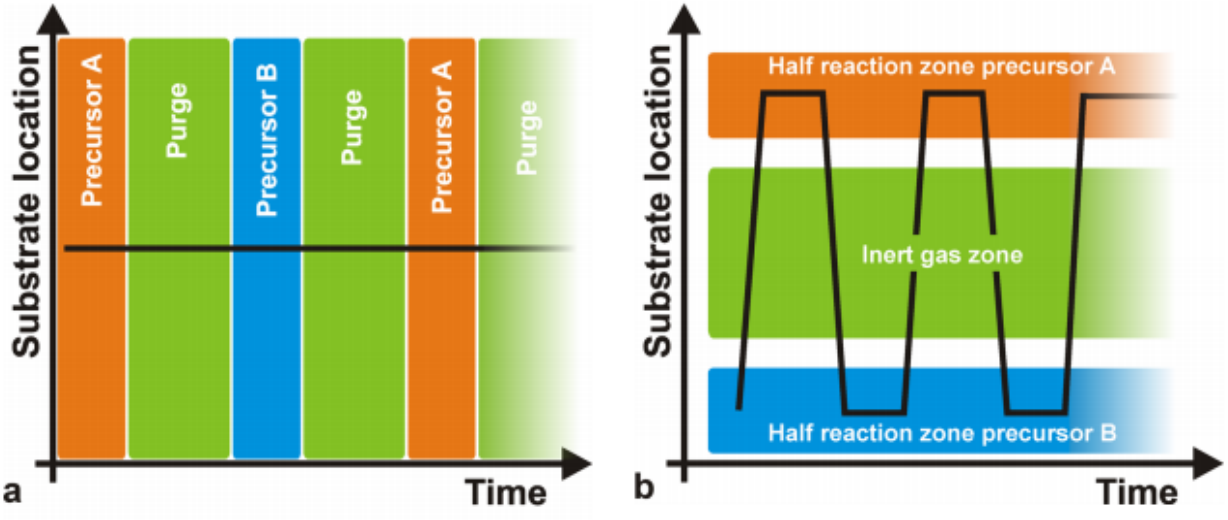

Figure 25: ALD process where variation of substrate position (black line) and time under different precursors is illustrated for (a) conventional ALD and (b) spatial ALD [95].

To achieve this, a SALD can use a specialized reactor head with different gas channels as seen in Figure 26a-b. Inert gas curtains separate the metal precursor from the oxygen precursor. Keeping the reactor head in close proximity to the substrate allows for the process to be carried out in atmosphere. These distances are kept close to ~100 μm creating a pressure gradient and

forcing the excess precursors into exhaust channels, which improves gas isolation while improving the uniformity of gas flows [96], [97]. The combination of proximity and inert gas barriers can effectively create a chamber that isolates the reactants from atmosphere and each other. If the gasses are not truly separated, reaction of the precursors in the gas phase and deposition on the heated substrate (chemical vapour deposition) occurs. The throughput of this process can be scaled by simply widening the reactor head and/or increasing the number of precursor channels. As the substrate passes under the reactor head multiple SALD cycles can occur. Figure 26 demonstrates two SALD cycles but specialized systems can complete an entire film in one pass.

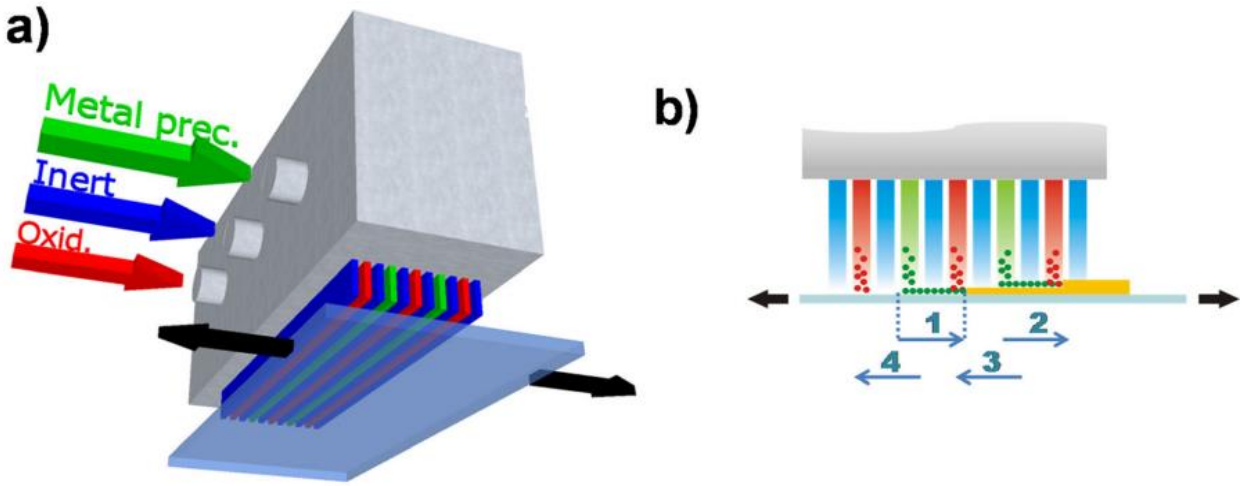

Figure 26: (a) Drawing of a spatial atomic layer deposition reactor head with a metal precursor (green) and oxygen precursor (red) separated by inert gas curtains (blue). (b) Side view representation of SALD coating process [98].

The precursors are held in airtight glass containers with Teflon lids as seen in Figure 27. These precursors are typically air or water sensitive, very flammable or pyrophoric [97]. Because of this, the precursor carrier must be very secure. Nitrogen continuously flows into the bubbler where the liquid precursor is bubbled into the gas phase and delivered to the reactor head through a carrier line. The flow of nitrogen to the bubbler can be controlled along with the flow in the

carrier line. These are independently controlled to change the concentration of precursor being delivered to the reactor head while maintaining a desired total flow rate.

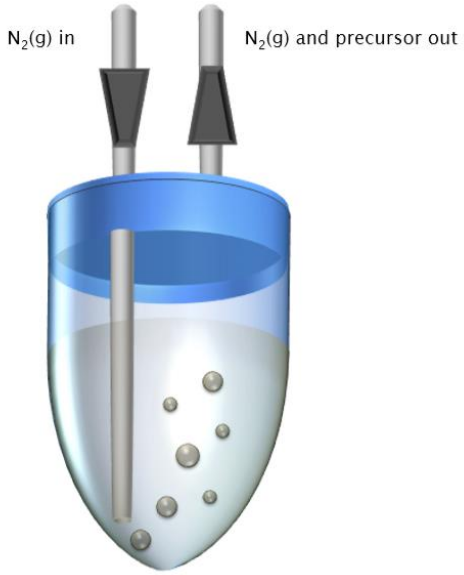

Figure 27: Schematic of glass bubbler used to vaporize precursors in AP-SALD [99].

4.3 Fabrication of WO_3 by ALD

Fabricating tungsten oxide by conventional ALD is not common in literature. Three precursors of interest are listed in Table 7. However, as the goal is to create crystalline or polycrystalline WO_3, some precursors can be eliminated. Dezelah et al. produced amorphous W_2O_3 using $W_2(NMe_2)_6$ making it unsuitable for this application [100]. Bis(tert-butylmino)bis(dimethylamino)tungsten(VI) (BTBMW) and tungsten hexacarbonyl are both viable options to produce WO_3. However, tungsten hexacarbonyl was reported to have a narrower growth window of 195-205°C and only produced partially crystalline films [101]. Oxygen deficient crystalline WO_3 was fabricated using BTBMW and H_2O as precursors [102], such that BTBMW may be a suitable precursor for the deposition of WO_3 films by AP-SALD for

perovskite solar cells. However, the deposition of WO_3 by AP-SALD has not previously been demonstrated.

Table 7: Summary of different precursors to produce tungsten oxide by ALD

Precursor A	**Precursor B**	**Deposition Temp**	**Product**	**Ref**
Bis(tert-butylimino) bis(dimethylamino)tungsten(VI)	H_2O	250-350°C	Oxygen deficient crystalline WO_3 Anneal at 550°C to remove O_2 deficiencies Precursor heated to 75°C	[102]
Tungsten Hexacarbonyl $W(CO)_6$	Ozone	195-205°C	Partially crystalline WO_3 Requires post annealing at 600-1000°C	[101]
$W_2(NMe_2)_6$	H_2O	140-240°C	Amorphous W_2O3	[100]

4.4 Experimental Conditions

4.4.1 Atmospheric Pressure Spatial Atomic Layer Deposition System

The custom-built AP-SALD system situated in a fume hood; a schematic can be seen in Figure 28a. Ultra high purity 5.0 nitrogen from a cylinder is sent to an array of mass flow controllers (MFCs) which control the flow of nitrogen being sent to the bubblers or carrier lines. The flow rate is quantified by standard cubic centimeters per minute (sccm). By increasing the flow of nitrogen to the bubbler, the concentration of vaporized precursor increases. The nitrogen and vaporized precursor travel to a carrier line where it is met by a higher flow of nitrogen and delivered to the reactor head.

The carrier line enters a manifold above the reactor head where it is split and delivered to different channels on the reactor head. Figure 28b shows a schematic of the system's reactor head and how the flow of gas in each channel is split. Each colour represents a different gas inlet. The blue lines indicate the path pure nitrogen flows which plays the role of inert gas curtains.

The nitrogen inlet is split across six channels. Metal 1 (red) is split into two channels and is rarely used in the system. The oxygen (orange) is also split into two channels and will typically carry water, ozone or hydrogen peroxide. Metal 2 (green) has one channel and is primarily used for depositions. There are ten exhaust channels (black) between each precursor and nitrogen curtain channel. To summarize, in the system detailed in this report, there are six nitrogen curtains, two oxygen channels and one metal channel (Metal 2) that are used to create films.

A substrate is placed on the stage, which is heated to a desired temperature and can oscillate over one axis. When the substrate oscillates forward then back under the reactor head, one oscillation or cycle is complete. The spacing between the reactor head and substrate is important in creating ALD growth. Three micrometers control the height of the reactor head. Metal shims of set thicknesses are used as a guide to lower the reactor head to a set height. Having the reactor head level to the substrate is important for keeping the flow of gas under the reactor head even/uniform. If one corner of the reactor head is tilted upwards relative to the other corners, a pressure gradient under the reactor head is formed making the flows non-uniform.

The user interface of the system can be seen in Figure 28c. The black lines indicate the path the gases travel. A series of pneumatic valves, manual valves and one-way valves prevent the back flow of oxygen to the bubbler/MFCs to protect them. The pneumatic valves also act as on/off switches between depositions. Through this display, the flow rates, substrate temperature, oscillation speed and number of oscillations can be set.

The metal precursor used in this experiment was Bis(tert-butylimino)bis(dimethylamino) tungsten(VI) (BTBMW) in the Metal 2 channel. The oxygen precursors used in this experiment were H_2O and ozone. Glass, silicon and indium tin oxide (ITO)-coated glass were used as substrates.

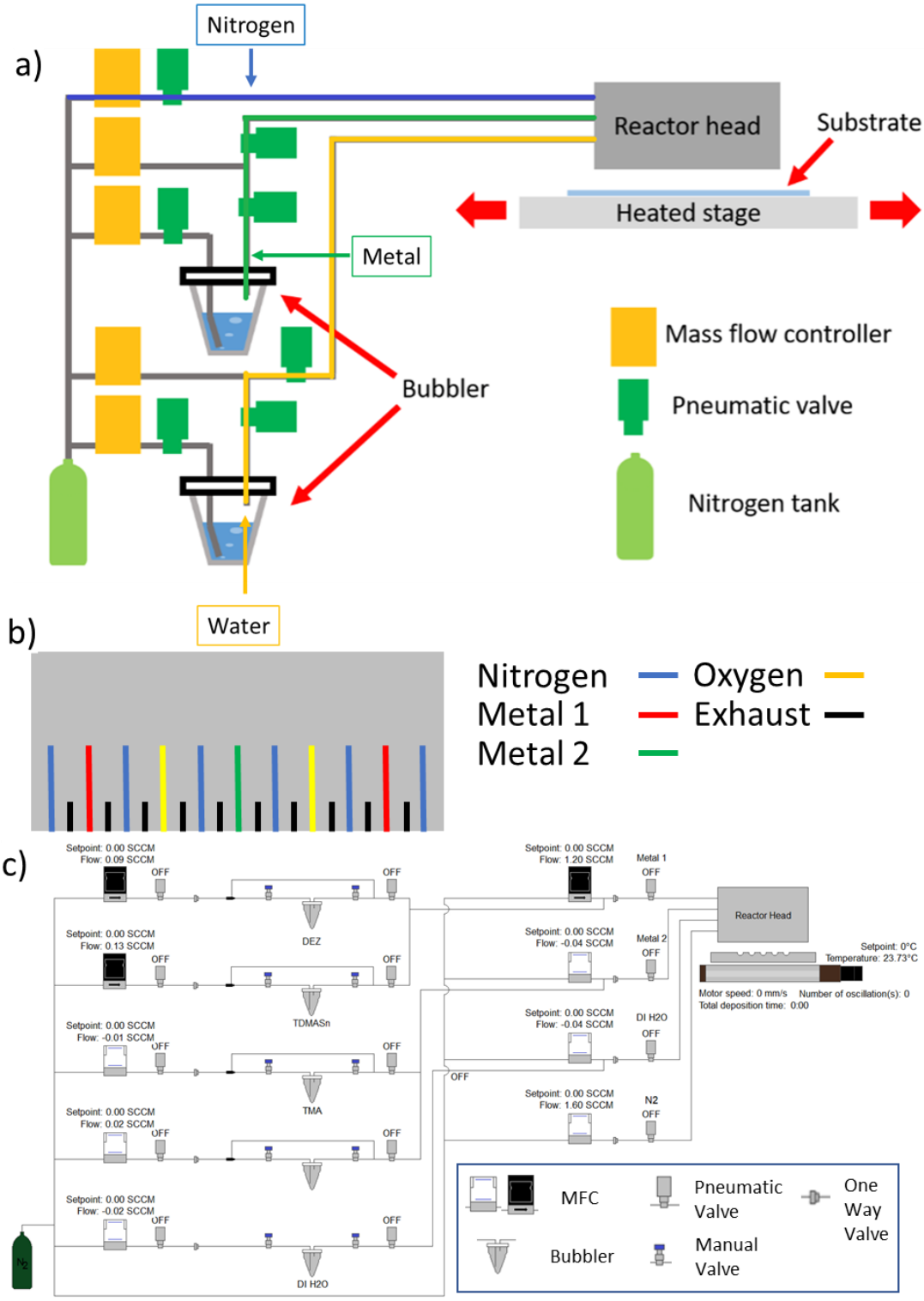

Figure 28: (a) Schematic of AP-SALD machine with (b) a schematic of the reactor head showing the flow of different carrier lines with Nitrogen (blue), Metal 1 (red), Metal 2 (green), Oxygen (yellow) and Exhaust (black). (c) The user interface of the AP-SALD system including a schematic of the tubing.

4.4.2 Addition of a Nebulizer and Ozone Generator to the AP-SALD System

While AP-SALD has many advantages over conventional ALD, it lacks a vacuum to assist in the vaporization of the liquid precursors, such that volatile precursors are typically used, which can be easily vaporized by bubbling with nitrogen. It was expected that the vapour pressure of BTBMW would be lower than common ALD precursors, as in the previous report of ALD of WO_3 using BTBMW, the precursor had to be heated to 75°C to produce a sufficient quantity of gas when bubbling [97]. This is problematic in that the boiling point of this precursor is 81°C and the flash point is 85°C. In preliminary trials with our AP-SALD system, heating of the BTBMW precursor to levels where deposition was possible was found to result in thermal degradation of the precursor. After a few sessions, the viscosity increased, and the precursor was reduced to a gel. This level of degradation is not suitable for producing consistent films.

To combat this, a nebulizer was implemented in our AP-SALD system. A nebulizer acts in a similar fashion as a humidifier. An ultrasonic element vibrates and agitates the precursor creating a mist of atomized particles. An optical sensor monitors the amount of liquid in the nebulizer, which must be kept constant to ensure the rate of atomization is consistent. If there is too much liquid then the nebulizer will be unable to atomize any liquid, too little and the rate increases. A valve automatically opens and closes depending on the optical sensor, which allows more precursor to enter the nebulizer from a reservoir. A 2.4 MHz 241PG particle generator from Sonozap seen in Figure 29 was used. The nebulizer has a built-in protection protocol causing it to shut down after prolonged depositions. This is to prevent the nebulizing element from overheating. At max power the nebulizer will pause after 30 minutes of operation for 15 minutes. The power of the nebulizer can be controlled in increments of 5% up to 100%. Since

the nebulizer can change the concentration of precursor atomized, a separate carrier/bubbler line is not required. The carrier line is connected directly to the nebulizer.

An air-tight teflon bottle was constructed to use as the precursor reservoir, which was held by a clamp. As shown in Figure 26, the container has an inlet to allow nitrogen to flow in and displace the missing volume as the precursor flows from the reservoir to the nebulizer. An exhaust is placed above the inlet to allow excess nitrogen to exit. This prevents pressure build-up in the reservoir.

The precursor BTBMW (1 mL) was dissolved in anhydrous toluene (100 mL) and inserted into the precursor reservoir in a nitrogen glovebox. Teflon tape was used to protect the body of the nebulizer from toluene that may spill on it since toluene will react with the plastic casing. After removing the nebulizer and precursor reservoir from the glovebox and attaching it to the AP-SALD system, a heating wire was wrapped around the precursor carrier line, which was heated to approximately 40^{o}C to prevent condensation of the precursor in the line. Implementation of the nebulizer was found to result in reliable delivery of the precursor to the AP-SALD reactor head, while safely avoiding heating of the precursor and precursor degradation. Additional metal precursors that benefit from this are niobium ethoxide to make Nb_2O_5 and titanium ethoxide to make TiO_2 films [99].

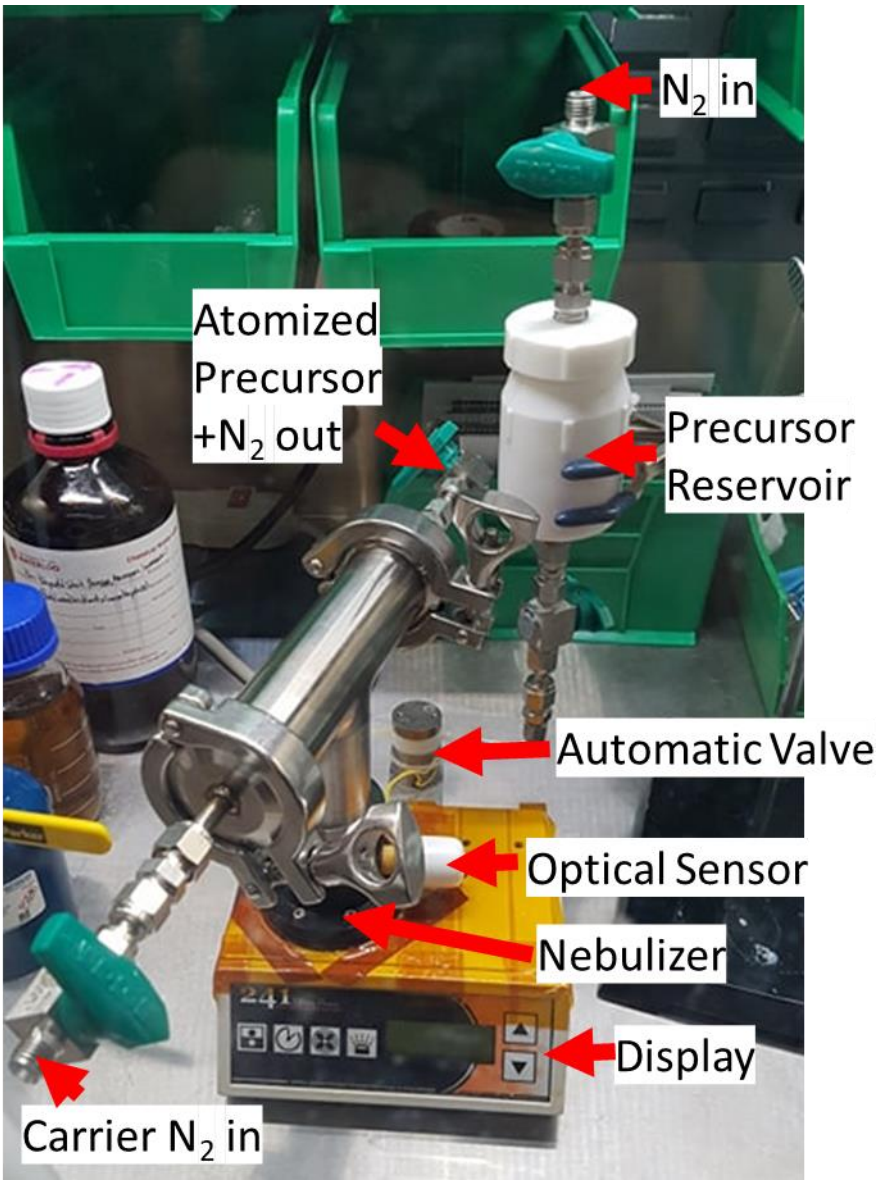

Figure 29: Labelled nebulizer

It was noted in Section 4.3 that previous work by Zhuiykov et al. on the deposition of WO_3 using BTBMW and H_2O resulted in oxygen deficient WO_3 [97]. This could potentially be remedied by using a more reactive oxygen precursor such as ozone or by increasing the water concentration. Also, a deposition temperature of 250-350°C was used in this previous report, which would prevent the integration of the WO_3 films into a PSC with a n-i-p structure, as the perovskite layer typically degrades at temperatures above 140°C [50], [82]. Again, the use of a

more reactive oxygen precursor may facilitate the WO_3 deposition at a lower temperature. When compared to water, ozone is known to reduce the deposition temperature for aluminum oxide [103]. The precursor, trimethylaluminum (TMA) and ozone produced films at temperatures as low as 50°C while H_2O could only produce films above 100°C [103].

To this end, an ozone generator was incorporated into the AP-SALD system. An ATLAS 30UHC ozone generator from Absolute Ozone was used to generate ozone from an oxygen gas cylinder with 7.5% nitrogen balance. A manual mass flow controller was placed at the output of the ozone generator to control the flow. This connects directly into the brass manifold above the reactor head in place of the oxygen carrier line. A dial was used to set the potentiometer of the ozone generator which affects the concentration of ozone generated. The system was calibrated to 20 psi. The ozone generator and mass flow controller are pictured below in Figure 30. It should be noted that the accuracy of the manual MFC is questionable due to the scale being in standard liters per minute (slpm) instead of sccm and the flow of gas typically being used was around 300 sccm.

Figure 30: Absolute Ozone, ATLAS 30UHC and mass flow controller

4.4.3 Characterization Tools

Film thickness was measured by DEKTAK and reflectance spectroscopy. To measure films by DEKTAK, additional samples of WO_3 on glass were etched with a 10% solution of HCl and zinc powder as a catalyst. A Dektak 8 stylus profilometer was used to measure the film thickness of 75, 150 and 225 oscillations samples.

An Ocean Optics HDX UV-Vis spectrometer was used to measure the thickness of a 450 oscillation WO_3 film on silicon. This tool was also used to characterize the optical properties such as the index of refraction and band gap. The results were fit to a Tauc-Lorentz model. Tungsten oxide has an indirect and allowed bandgap transition [86]. The reflectance spectroscopy measurements and fittings were completed by Kissan Mistry (PhD).

A Zeiss Leo 1530 and UltraPlus FESEM (with EDX/OIM) scanning electron microscope (SEM) with energy-dispersive x-ray spectroscopy (EDX) was used to image a 450 oscillation WO_3 film on silicon and to characterize the elemental composition.

A Renishaw micro-Raman spectrometer was used to characterize the structure of a 450 oscillation WO_3 film on silicon. Measurements were made from 100-1000 cm^{-1} using a 633 nm red He-Ne laser. The measured samples were as deposited, after 200°C anneal for 1 hour and after 450°C anneal for 1 hour.

A PANalytical X'Pert Pro MRD HR-XRD was used for grazing incidence x-ray diffraction (GI-XRD). Measurements were made between 20° and 90° to characterize a 450 oscillation WO_3 film on silicon. The measured samples were as deposited, after 200°C anneal for 1 hour and after 450°C anneal for 1 hour. PANalytical X'Pert HighScore matching software was used to match the XRD results to data in the JCPDS powder diffraction database.

4.4.4 Creating Perovskite Solar Cells

Preliminary trials at implementing WO_3 films into perovskite solar cells were attempted. An inverted p-i-n architecture was used to create a glass/ITO/WO_3/Perovskite/PCBM/LiF/Al structure similar to Masi et al. [88]. WO_3 was deposited over glass substrates with ITO coatings by AP-SALD. After deposition of WO_3, the samples were sonicated in isopropanol for 15 minutes to remove any particles that may have fallen on the substrate then dried at 100°C for 15 minutes to remove any residual organics from the precursor. An anhydrous stock solution of 1.4 M lead iodide (PbI_2), 1.25 M formamidinium iodide (FAI), 0.0987 M cesium iodide (CsI) in dimethylformamide (DMF) and 0.0833 M guanidinium iodide (GAI) in DMSO were mixed together at 76%/24% (DMF solution/DMSO solution). 50 μl of perovskite solution was dropped on the sample and spin coated at 1000 RPM for 10 seconds then 6000 RPM for 20 seconds. When there were 5 seconds remaining, 300 μl of antisolvent (50%/50% chlorobenzene/chloroform) was dropped on the center of the substrate. After depositing the perovskite, the samples were baked at 140°C for 30 minutes then cooled to room temperature. Phenyl-C_{61}-butyric acid methyl ester (PCBM) is used as the electron transport layer and was dissolved at 25 mg/1 ml in chlorobenzene then spin coated at 1000 RPM for 60 seconds. 0.5 nm of LiF was thermally evaporated as a passivation layer then 100 nm of aluminum as the top electrode. Evaporation was carried out by Angstrom Engineering.

4.5 Deposition and Characterization of AP-SALD WO_3

4.5.1 Determining AP-SALD Parameters for the Deposition of WO3

Atmospheric pressure spatial atomic layered deposition has many parameters that can be altered to effectively make a film. This includes reactor head and substrate spacing, substrate temperature, substrate oscillation speed, number of oscillations, oscillation distance, flow rates

and precursor concentrations in the nitrogen carrier gases. With a nebulizer, the nebulization power can be changed to increase the precursor concentration. Likewise, the output power of the ozone generator can be increased to increase the ozone concentration. Generally, the total flow rate per channel was kept the same to prevent turbulent flow and precursor mixing under the reactor head.

The spacing between the reactor head and substrate was kept around 50 μm. The accuracy of leveling is questionable because high temperatures are required to deposit WO_3. At elevated temperatures the substrate, stage and reactor head experience thermal expansion. Shims that are typically used for leveling begin to decompose. All comparisons have trials done on the same day to limit the variability in experiments. The oscillation speed was kept low at 3 mm/s to allow for the precursor to saturate the substrate. Faster speeds displayed an incomplete film with very little deposition in the center. The oscillation path was kept at 20 mm. This meant 150 oscillations would take approximately 30 minutes, which is the duration the nebulizer could be left on. The nebulizer was set to 80% power. Below 80%, no films could be observed, suggesting insufficient BTMBW precursor in the gas phase. The ozone generator was set to 80%. At flow rates below 400 sccm, there is no accurate ozone concentration values since the ozone generator was only calibrated between 400 sccm to 3000 sccm.

Different flow rates in the channels of the reactor head were investigated. Figure 31 compares the films deposited on borosilicate glass under different flows per channel. At 100 sccm per channel, not enough precursor was being delivered to the substrate which is seen by the faded film. Judging by the sharp edges of the film, the growth mode appears to be ALD (i.e. the precursors are not mixing in the gas phase and resulting in chemical vapour deposition). At 300 sccm per channel, there appears to be turbulent flow under the reactor head, which can be seen

by the faded double lines at the top and bottom of the film indicating CVD growth. This is highlighted by the black lines in Figure 31. The flow rate of 150 sccm appears to be a good compromise between the two. It should be noted that there was a small blockage in one of the lines during these depositions, resulting in the faded line in the center of the film.

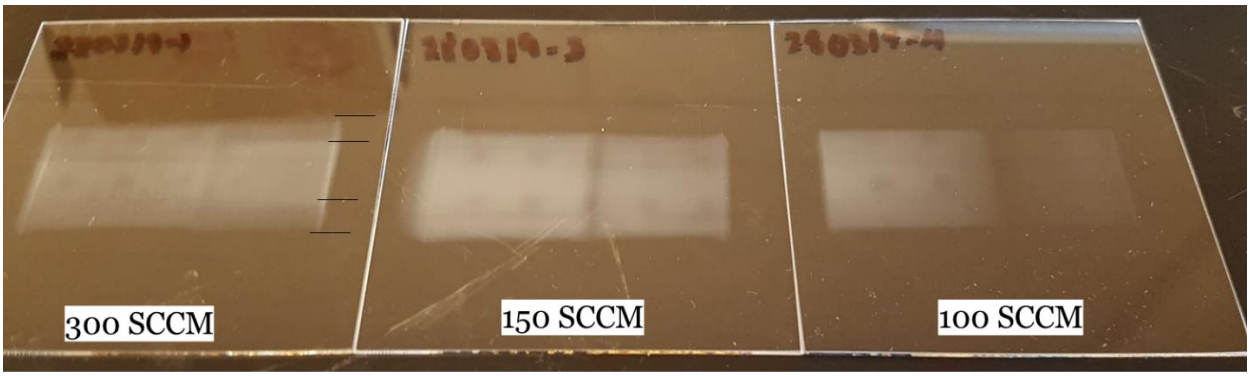

Figure 31: Comparing the uniformity of films under different total flow rates after 150 oscillations. At 300 sccm, indications of turbulent flow are highlighted by the black dashed lines

The effect of using ozone instead of water as a precursor was examined next. The parameters of these depositions are detailed in Table 8 which include the substrate temperature, number of oscillations, oscillation speed, nebulizer power, metal carrier (nebulizer) flow rate, ozone power, ozone/oxygen carrier flow rate, water bubbler and carrier flow rate, nitrogen curtain flow rate, heating tape temperature and the oscillation path width respectively. The films shown in Figure 32a-c align with the parameters in Table 8. As seen in Figure 32a, there is a very thick and uniform film grown on silicon using the ozone. After 450 oscillations the film is a blueish yellow. On the edges the film is thicker from excess precursor being pushed out the sides of the reactor head and reacting with oxygen and water in the atmosphere. Changing the precursor to water results in poor film growth, as shown in Figure 32b. Even after increasing the number of oscillations from 450 to 750 the film is a very light brown with the silicon substrate still visible underneath. Figure 32d and e examine the resulting powder formed on the underside

of the reactor head for depositions with ozone and water, respectively. When ozone is used, the powder is white throughout whereas when water is used the powder is black and white on the edges. The fact that all of the power on the head in Figure 32d is white when ozone was used (indicating reaction of the precursors to form WO_3) shows that the precursor gases are not perfectly isolated from each other. The black color is an indication that the water does not react as readily with the tungsten precursor (WO_3 powder is not formed). Excess precursor is forced to the exhaust channels and out the side of the reactor head. Out the sides there is more precursor mixing and exposure to atmosphere. This explains why the powder in Figure 32e is black in the center and white on the edges. The water was bubbled at the limits of the system (100 sccm through the bubbler and 200 sccm through the carrier) under these deposition parameters. Zhuikov et al. noted that when depositing WO_3 by ALD, the H_2O pulse time is longer than what is used in typical oxide growths indicating challenges with water saturation [102]. This shows that water is not a suitable precursor for tungsten oxide depositions in this AP-SALD system. A slower oscillation speed could provide the required saturation time at the cost of deposition time.

Table 8: Deposition conditions for tungsten oxide films comparing temperature and water/ozone precursors

Film	**Temp**	**Osc.**	**Speed**	**Neb. Power (%)**	**Metal Carrier (sccm)**	**Ozone Power (%)**	**Ozone flow (sccm)**	**Water Bubbler (sccm)**	**Water Carrier (sccm)**	**N_2 Curtain (sccm)**	**Heat Tape Temp**	**Osc. Path**
WO3 + Ozone	350°C	450	3 mm/s	80	150	80	300			900	40°C	20 mm
WO3 + Water	350°C	750	3 mm/s	80	150			200	100	900	40°C	20 mm
WO3 + Ozone	330°C	450	3 mm/s	80	150	80	300			900	40°C	20 mm

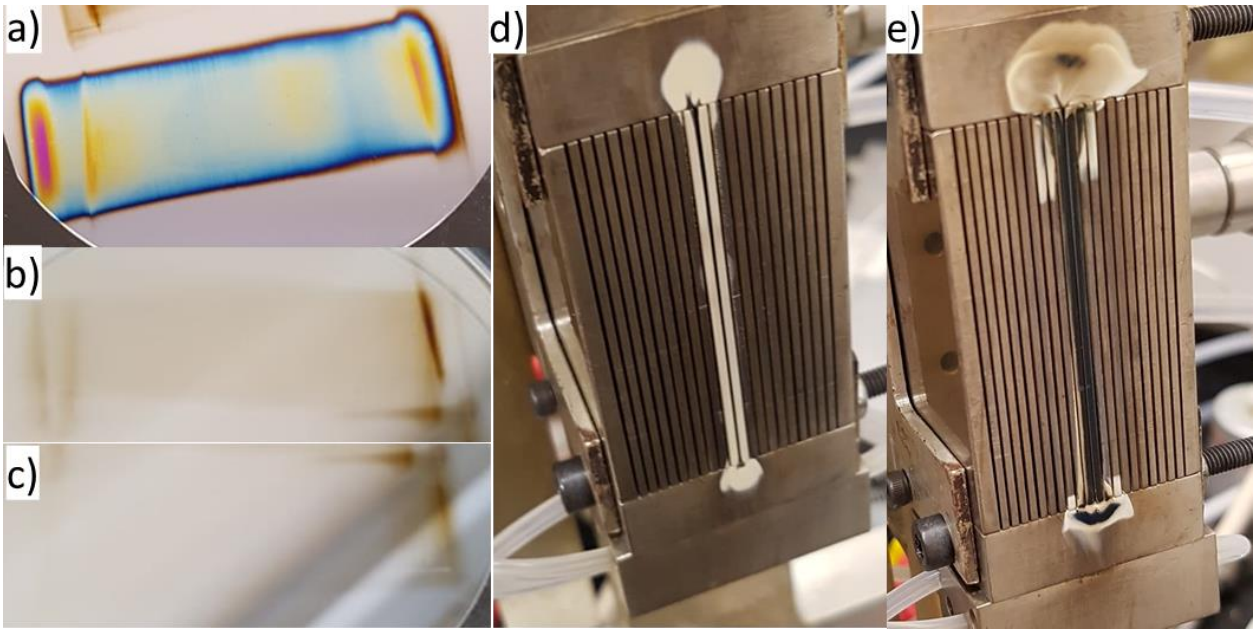

Figure 32: Comparing the films of (a) a standard deposition (450 oscillations), (b) using water instead of ozone (750 oscillations), (c) a lower temperature of 330°C instead of 350°C. The residual powder from a deposition is also compared between (d) standard conditions and (e) with water instead of ozone.

Figure 32a and c compare the effect of the substrate temperature. All parameters were kept the same except a 20°C reduction in temperature from 350°C to 330°C. There is a significant reduction in growth rate. Although not shown, the resulting powder on the underside of the reactor head is identical to Figure 32d. This confirms the influence of ozone while highlighting the temperature dependence of this process. The higher growth rate observed at 350°C versus 330°C aligns with Zhuiykov et al.'s findings as seen in Figure 33. Unfortunately, the low growth rate observed at 330°C suggests that the use of ozone does not significantly increase the deposition window for this process to lower temperatures. As will be discussed later, this limits the potential usage of AP-SALD WO_3 in perovskite solar cells.

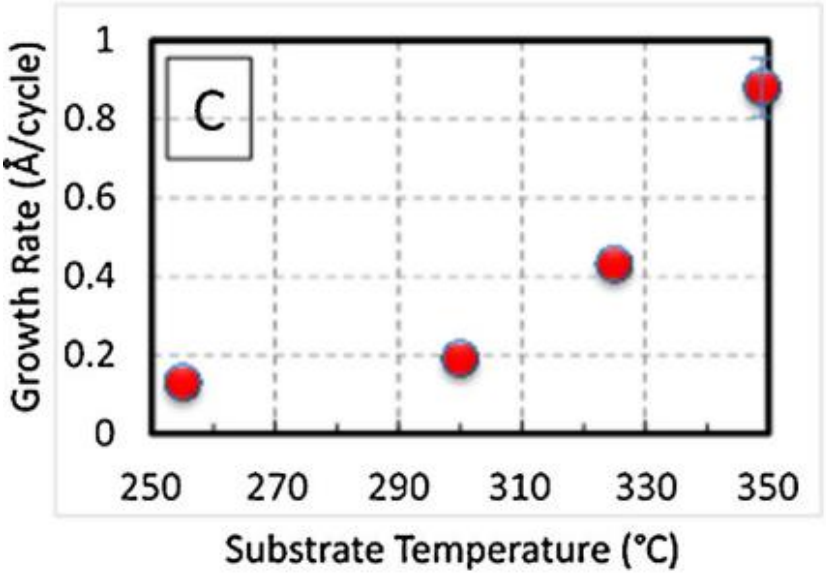

Figure 33: Previously-reported growth rate per cycle in ALD deposition of tungsten oxide using precursors BTBMW and H_2O [102].

All WO_3 films characterized in this report were deposited on silicon using conditions listed in Table 8 row 1 unless otherwise stated. After deposition, the samples were sonicated in isopropanol for 15 minutes then dried at 100°C for 15 minutes. In some cases, where noted, the films were annealed for 1 hour at 200°C or for 1 hour at 450°C.

4.5.2 DEKTAK and Reflectance Spectroscopy

The film thickness was measured using a DEKTAK profilometer and by reflectance spectroscopy. Figure 34a-c shows three WO_3 films deposited on ITO substrates using 75, 150 and 225 oscillations. These films were measured by DEKTAK and determined to be 171 Å, 368 Å and 609 Å respectively. The film in Figure 32a was measured by reflectance spectroscopy and determined to be 1060 Å as seen in Figure 35a. The film thickness as a function of the number of AP-SALD oscillations is plotted in Figure 34d. A linear film growth is observed that is independent of the substrate. A growth rate of 2.4 Å/oscillation is determined which is equivalent to 1.2 Å/cycle (since one oscillation involves the substrate moving forward and back under the

reactor head). Zhuiykov et al. observed a growth rate of 0.87 Å/cycle (monolayer) in a standard ALD system [102]. The larger growth rate of roughly 1.5 monolayers/cycle suggests CVD growth is occurring, consistent with the precursor mixing observed in Figure 32d.

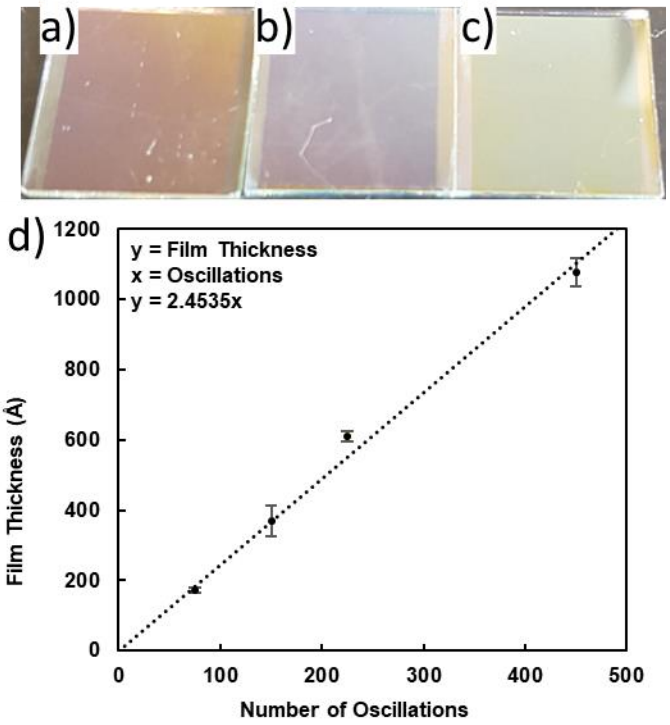

Figure 34: Tungsten oxide deposited on ITO substrates using (a) 75, (b), 150 and (c) 225 AP-SALD oscillations. (d) The growth rate is determined by plotting as a function of film thickness (y) vs number of oscillations (x). The points at 75, 150 and 225 oscillations were measured by DEKTAK and the point at 450 oscillations was measured by reflectance spectroscopy

The refractive index, extinction coefficient and bandgap of a 450 oscillation film were obtained from the fitted reflectance spectroscopy data and are shown in Figure 35b-c. Charles et al. deposited monoclinic WO_3 by DC sputtering and determined a refractive index of $n_{589\ nm}$ = 2.18 and a band gap of 3.05 eV [104]. Valyukh et al. also created a monoclinic WO_3 film by DC sputtering with a refractive index of $n_{589\ nm}$ = 2.01 and a bandgap of 3.15 eV [105]. Other reports show that the band gap of WO_3 powder produced by oxidation of tungsten powder is close to 3.25 eV [106], [107]. Typically, band gaps for WO_3 thin films are >3eV and 2.62 for bulk WO_3

[104], [108]. In this case, the band gap was recorded to be 3.27 eV and the refractive index to be $n_{589\ nm}$ = 2.36. The bandgap in this study agrees with the reported literature while the refractive index values are a bit larger than expected. This could be due to a more compact film (free of voids), as might be expected for layer-by-layer growth of films [109].

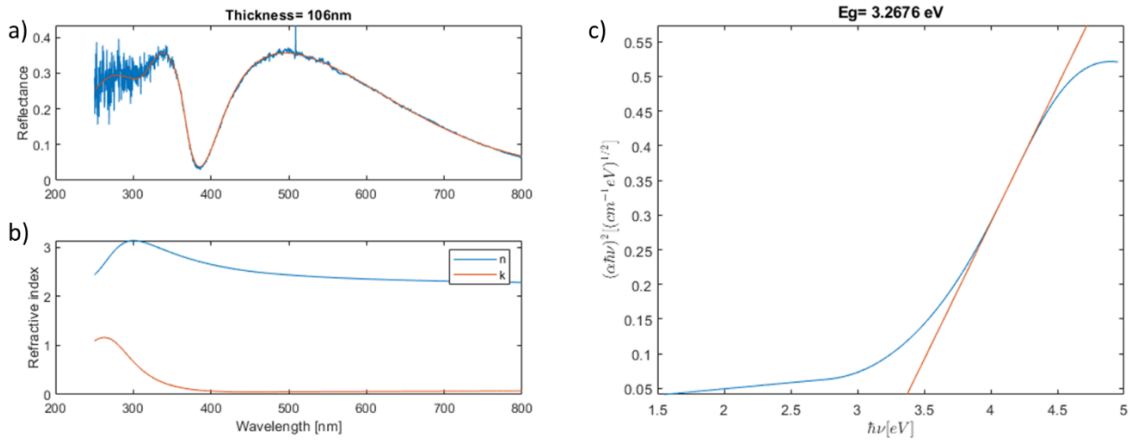

Figure 35: Reflectance spectroscopy results showing the (a) fitted film thickness, (b) refractive index and extinction coefficient and (c) the band gap of a WO_3 film on silicon after 450 oscillations

4.5.3 SEM + EDX

Tungsten oxide films deposited on silicon were examined by a scanning electron microscope with energy-dispersive x-ray spectroscopy. Figure 36a-c examines the 100nm thick tungsten oxide film deposited on silicon at 5K X, 20K X and 30K X magnifications respectively. At 5K X, a smooth film and occasional spherical particles are seen. At 30K X an agglomerate of these particles is examined. The particles are spherical in shape. When powder builds up on the reactor head over sequential depositions without cleaning, powder is observed on the substrate. If the reactor head is cleaned, there is less observable powder. Agglomerations of particles on the reactor head could fall onto the substrate resulting in what is observed in Figure 36b. This shows some indication of CVD growth or some of the atomized precursor condensing within the

system. At 100K X, the grains of the uniform film can be seen. Figure 36d-e compares the EDX spectra of the deposited WO_3 film and a WO_3 film deposited by conventional ALD found in literature. The tungsten and oxygen peaks found are comparable to literature. A small peak at ~3.5 eV is attributed to the silicon double peak from the substrate. The presence of silicon also influences the EDX results since the silicon forms an oxide layer on the surface. Zhuiykov et al. was able to observe stoichiometric tungsten oxide by EDX with 75.97 and 24.03 atomic % of oxygen and tungsten respectively. This rounds to the desired stoichiometry of one tungsten atom per three oxygen atoms [102]. The presence of silicon increases the atomic % of oxygen making the EDX values unreliable for determining stoichiometry. Still, EDX can confirm the presence of only tungsten and oxygen in the film.

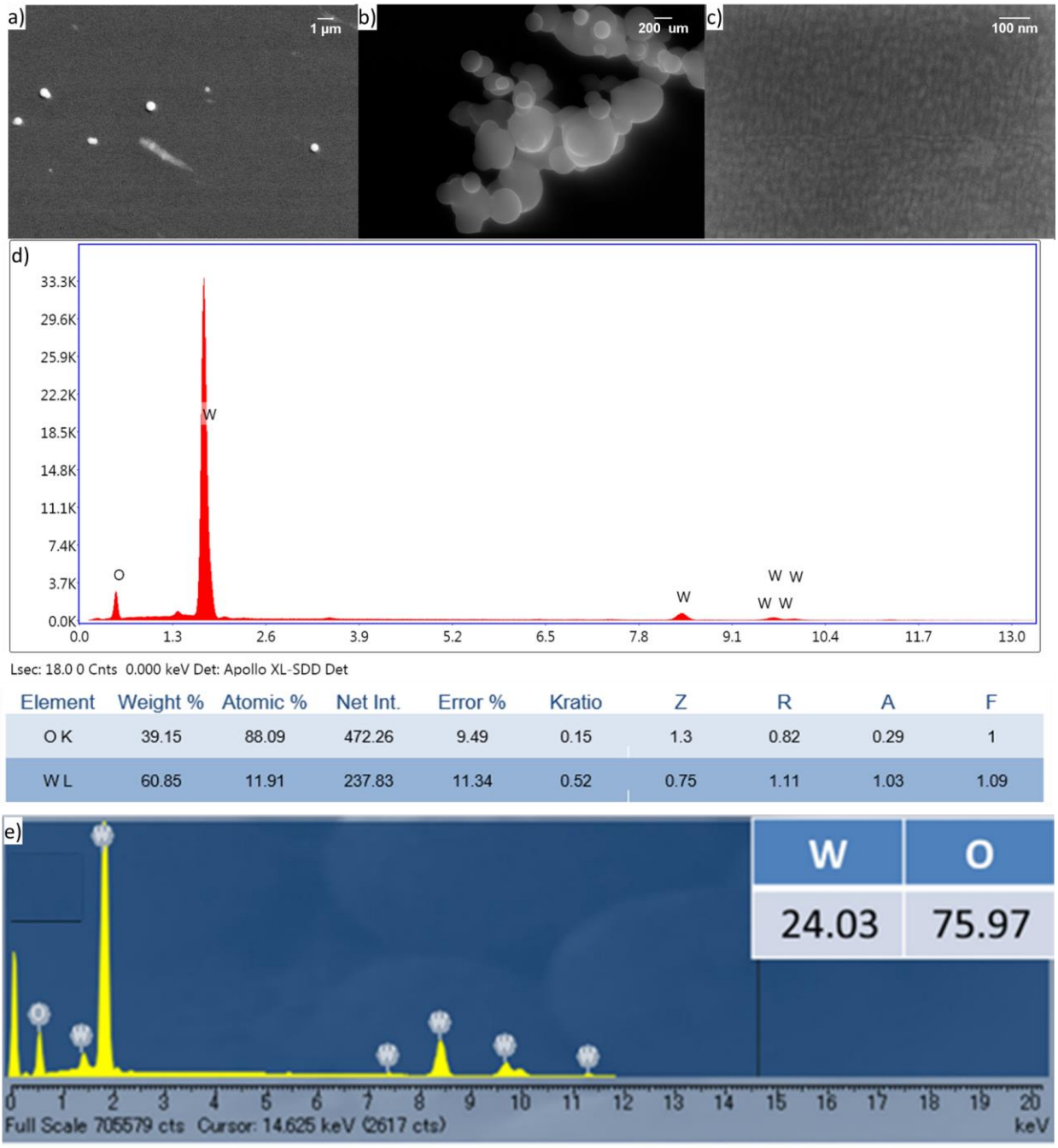

Element	Weight %	Atomic %	Net Int.	Error %	Kratio	Z	R	A	F
O K	39.15	88.09	472.26	9.49	0.15	1.3	0.82	0.29	1
W L	60.85	11.91	237.83	11.34	0.52	0.75	1.11	1.03	1.09

Figure 36: SEM images of 100 nm thick WO_3 film deposited on silicon. (a) Shows the surface of the film at 5K X magnification, (b) particle agglomerates at 30K X magnification and (c) individual grains at 100K X magnification. (d) EDX results of the film surface are reported along with (e) EDX of a comparable WO_3 deposited by conventional ALD from literature [102].

4.5.4 Raman Spectroscopy

Figure 37a shows the Raman spectrum of a WO_3 film deposited on silicon. The film was examined after deposition, after annealing at 200°C for 1 hour in atmosphere on a hot plate, and after a 450°C anneal for 1 hour in atmosphere. Plain silicon was also measured to distinguish the tungsten oxide from the silicon. Silicon peaks are observed at 301, 428, 510 and 940 cm^{-1}, consistent with literature [110]. The spectra for the as deposited and the 200°C annealed WO_3 films are similar. Peaks are identified at 134, 676 and 805 cm^{-1} which align with a metastable water saturated hexagonal WO_3 ($WO_3 \frac{1}{3} H_2O$) [111]. Baking at 200°C was reported to be sufficient to induce a phase change to monoclinic WO_3 [111] but the similar spectra observed here indicate the temperature is not high enough to induce the phase change in the films. These results are different from the Raman spectra of monoclinic WO_3, as shown in Figure 37b. It is found that after annealing at 450°C a new peak is formed at 267 cm^{-1} and the peak originally at 676 cm^{-1} begins to shift to a larger value of about 710 cm^{-1}. These changes align with the Raman spectrum of monoclinic WO_3 found in literature [102]. Figure 37b also identifies a peak at 324 cm^{-1} which may be masked by the silicon peak in this case. It should be noted that Zhuiykov et al. annealed their WO_3 films deposited by ALD at 550°C before examination [102]. Unfortunately, the limitations of the hot plate do not allow for such temperatures. A longer anneal or an oven may be more ideal. A UV laser is also recommended to hide the silicon peaks and make the WO_3 peaks easier to identify.

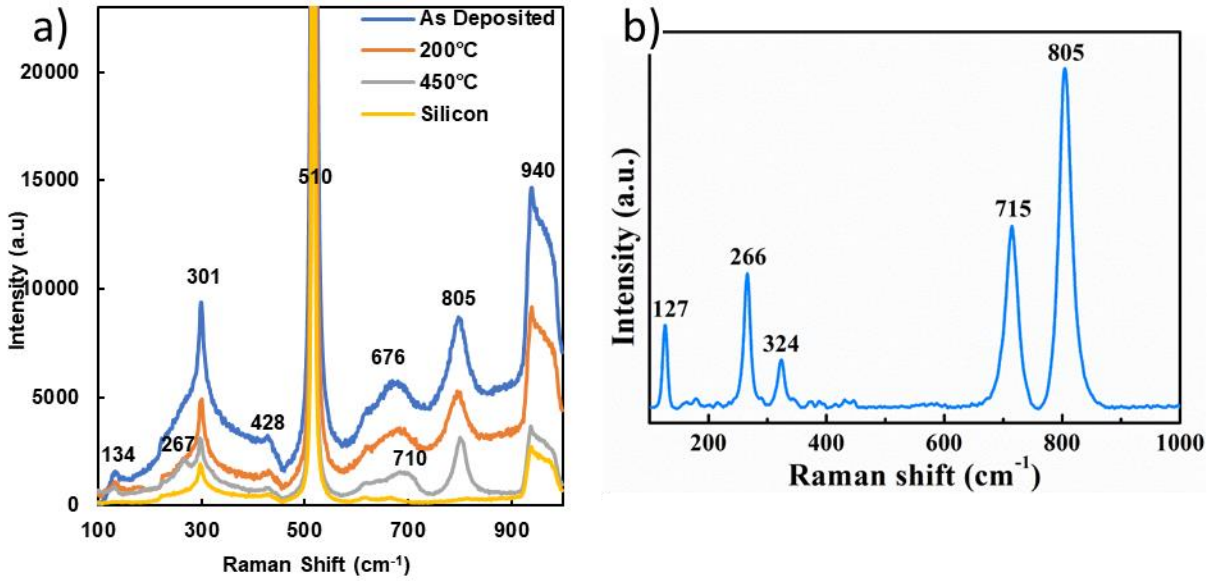

Figure 37: Raman spectra of (a) 100 nm thick WO_3 film deposited on silicon as deposited, after 1 hour of 200°C annealing and after 1 hour of 450°C annealing. A bare silicon sample is also measured to help identify the tungsten peaks. (b) A comparable WO_3 deposited by conventional ALD from literature [102].

4.5.5 XRD

Figure 38a shows the GI-XRD spectra of a WO_3 film deposited on silicon. Monoclinic WO_3 peaks (JCPDS-01-083-0950) and hexagonal $WO_3 \frac{1}{3}H_2O$ peaks (JCPDS 351001) are highlighted. The film was examined after deposition, after a 200°C anneal for 1 hour in atmosphere and after a further 450°C anneal for 1 hour in atmosphere. The intensity of each peak increased after each annealing period. This indicates a higher degree of crystallinity within the film. There are two additional peaks in the 450°C spectrum at 35° and 39°, which could indicate the beginning of a phase change. Contrary to the Raman spectroscopy results, the as deposited, and 200°C anneal films were all identified as monoclinic instead of hexagonal by the X'Pert HighScore matching software. Figure 38b shows the stick plots for all three spectra along with the matched monoclinic WO_3 results. The software gave a match score for the as deposited,

200°C anneal and 450°C anneal, of 62%, 62% and 67% respectively as monoclinic WO_3. Balázsi et al. has noted a peak at 18° that disappears after heat treatment of h-WO_3 $\frac{1}{3}$ H_2O [112], [113]. Unfortunately, the range of these results do not include this peak. Future measurements should extend to 10°. Nalwa et al. has noted that the exact phase identification in thin film WO_3 samples are difficult to identify due to the many WO_3 phases since each structure differs by a small amount [114]. It is likely the as-deposited film consists of a mixture of hexagonal and monoclinic WO_3 and annealing increases the proportion of monoclinic WO_3 [113].

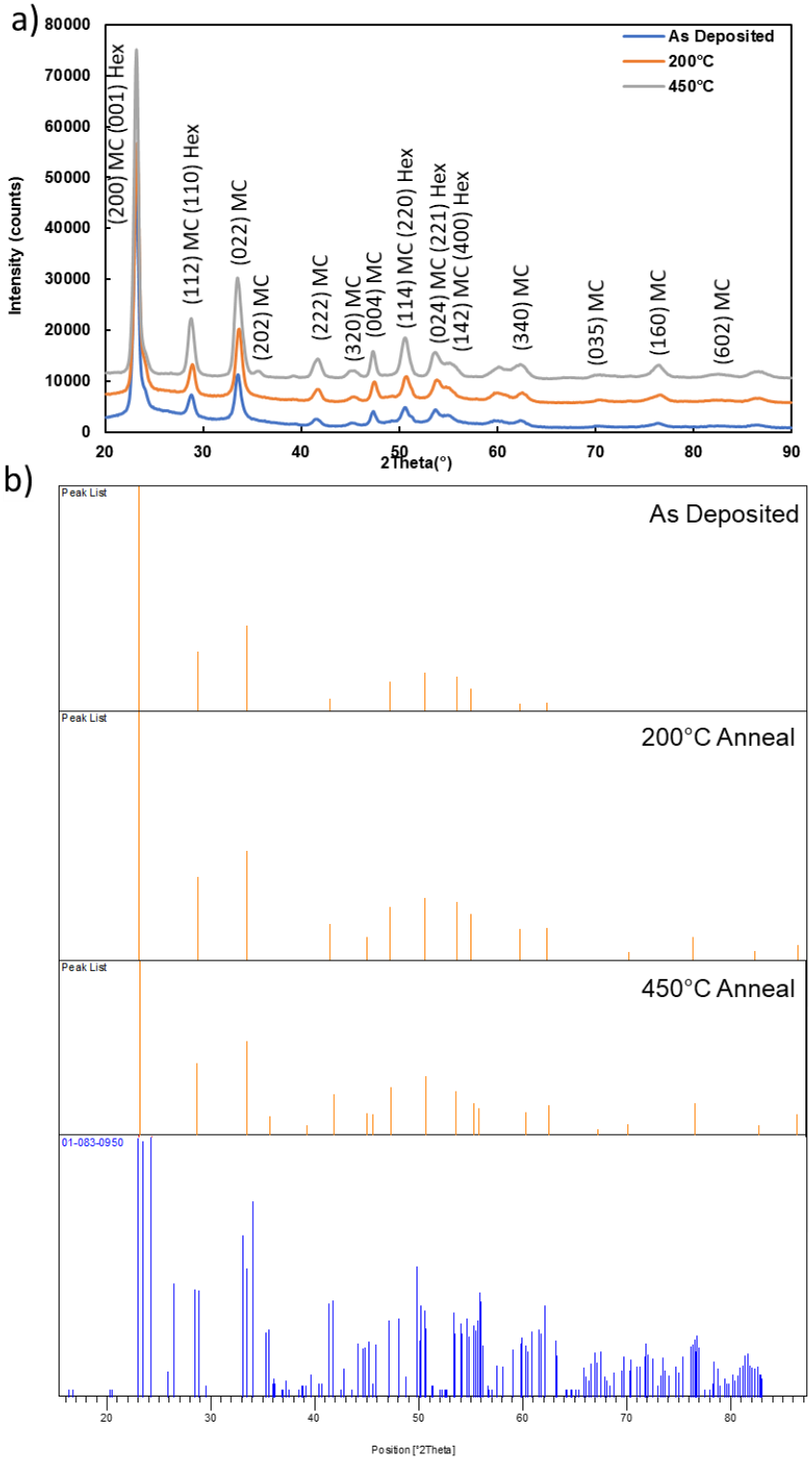

Figure 38: (a) GI-XRD spectra of 100 nm thick WO_3 film deposited on silicon as deposited (blue), after 1 hour of 200°C annealing (orange) and after 1 hour of 450°C annealing (gray) and (b) stick plots comparing the three films to the best match by the X'Pert HighScore software

4.6 Implementing in Perovskites

WO_3 was deposited over glass substrates with ITO coatings using deposition parameters detailed in Table 8 row 1. The AP-SALD parameters used to fabricate the WO_3 films limit the available architectures of perovskite solar cells. Tungsten oxide requires deposition temperatures of 350°C. This prevents WO_3 from being a layer on top of the perovskite absorber, as this temperature would rapidly degrade the perovskite material. If WO_3 is to be used as a hole transport layer, an inverted p-i-n architecture is required. As mentioned in section 4.2, Sofia et al. created p-i-n devices with the architecture, ITO/WO_3/Perovskite/PCBM/LiF/Al [88]. A lithium fluoride layer is placed between the PCBM and Al to prevent shunt paths from forming between the Al electrode and the perovskite layer since the PCBM layer is very thin [87], [115]. The film thicknesses were optimized to 40 nm of WO_3 and PCBM, 0.5 nm of LiF and 100 nm of Al [88]. It should also be noted that ITO films thermally degrade at elevated temperatures. It was previously reported that when annealing at 200°C, the resistivity and optical transmittance of the ITO begins to increase. The optical transmittance saturated at 300°C and the resistivity at 400°C. The films in this previous work were heated for 100 hours in air so the extent of degradation for shorter periods must still be examined if ITO is to be used in p-i-n WO_3 perovskites [116].

Preliminary attempts at implementing AP-SALD deposited WO_3 films in perovskite solar cells have been made. No devices were successfully completed due to issues detailed below. A few suggestions for improvement are as follows:

- 15 minutes of sonication in isopropanol was done after deposition of the WO_3 but particles are still seen on the substrate via SEM. Extended sonication times should be attempted.

- WO_3 particle build-up on the reactor head intensifies after prolonged depositions. Depositions should be done in 15-minute sessions with the reactor head being wiped and cleaned during each break.
- Monoclinic WO_3 is desired for the HTL in perovskites. A 450°C anneal for 1 hour appears to enhance this phase in the material. Extending the anneal to 3 hours or annealing at 550°C could improve this.
- Issues with the perovskite layer wetting the WO_3 layer were encountered. When the perovskite solution was drop-cast onto the HTL for spin coating, the perovskite solution beaded up and did not provide uniform surface coverage. This is a common issue with metal oxide HTLs in inverted p-i-n devices [117], [118]. UV-ozone treatment is found to improve the wetting properties. 15 minutes in the ozone-cleaner may improve the wettability without affecting the performance.

4.7 Conclusions

AP-SALD is a promising technique to produce metal oxide thin films in a scalable way. Further development of this technique by implementation of a nebulizer and ozone generator extends the list of metal oxides that can be created by facilitating the use of more precursors. The consistency with which films can be produced also improves in situations where the precursor needs to be heated to reach the vapour phase. The concentration of precursor delivered to the reactor head can be increased in cases where substrate saturation is poor by using a nebulizer. An ozone generator produces a more reactive precursor than a traditional water bubbler.

For the first time, mixture of hexagonal/monoclinic WO_3 phases were fabricated by AP-SALD at a growth rate of 2.4 Å/oscillation or 1.2 Å/cycle. The growth rate indicates CVD growth rather than ALD which is also evident by particles on the film surface in SEM images.

The band gap and index of refraction are consistent with what is found in literature. Raman spectroscopy and XRD indicate a combination of hexagonal and monoclinic WO_3 which becomes increasingly monoclinic via annealing.

Due to the required deposition temperature, an inverted p-i-n structure is required if these AP-SALD WO_3 films are to be used in perovskite solar cells. Preliminary attempts indicate the wettability of this layer as an issue that can easily be remedied by placing the samples in an ozone cleaner for 15 minutes. Further attempts should be made at completing this device.

5.0 Outlook

Photovoltaics are an exciting and practical technology that can drastically affect the world in a positive way. Clean renewable energy has the potential to supply all energy demands if improvements can be made to the scalability of the technology. The most effective way to increase adoption is to reduce cost. The most obvious way would be to reduce the manufacturing costs but improvements in energy conversion efficiency and device lifetime are also methods to reduce cost. The standard for photovoltaic modules is a lifetime of 25 years. To achieve this, different methods for identifying degradation can be applied along with new solar cell architectures and manufacturing methods.

Impedance spectroscopy is a powerful technology that can non-invasively characterize and quantify different degradation modes within a solar cell or module. Traditional characterization methods are used to identify a specific type of degradation. Multiple tools must be combined to paint a full picture of the device's state. Here, impedance spectroscopy was used to identify CID and PID in PERC modules. CID was examined by observing a decrease in minority carrier lifetime while PID was examined by a dramatic reduction in shunt resistance. The type of PID was also identified as PID-p instead of a more common PID-s based on the information a constant phase element provides. The extent of change is used to quantify the degradation when compared to a control module. A correlation between PCE and minority carrier lifetime was also found. The effect of a current induced regeneration process and silicon quality on CID in PERC cells was also examined by impedance spectroscopy. It was found that the CIR process plays a large role when preventing CID whereas the quality of silicon did not provide clear results. This technology should be applied to evaluate more modes of degradation

particularly in the field where a large array of tools are not available. Identifying degradation is the first step in improving the cost efficiency of photovoltaics.

Scalable manufacturing techniques such as AP-SALD can be used to quickly create high-quality, uniform, pin-hole free films. Even though there has been interest in this technology for a while, more progress must be made to reach commercial scales. This involves improving the capabilities and consistency while finding practical applications. A nebulizer and ozone generator were implemented in an AP-SALD system to expand the list of available precursors. BTBMW and ozone were used in conjunction to create hexagonal/monoclinic-WO_3 films for the first time by AP-SALD. The WO_3 films were characterized by DEKTAK, reflectance spectroscopy, SEM and EDX, Raman spectroscopy and XRD. This confirmed the growth rate, band gap, consistency and structure of the film. Attempts at annealing showed an increase in the monoclinic phase over the hexagonal. These films have great potential in perovskite solar cells. A new emerging photovoltaic technology that overcomes the expensive manufacturing costs of traditional silicon photovoltaics paired with a new, scalable manufacturing technique has the potential to disrupt industry. Further efforts must be made to implement AP-SALD films in perovskite devices.

Overall, the future of photovoltaics is very exciting. Emerging technology continuously pushes the field forward. A world powered by green energy may seem far, but the combined efforts of scientists brings us closer everyday.

6.0 References

[1] McKinsey, "Global Energy Perspective 2019," *Energy Insights*, no. January, 2019.

[2] S. K. Deb, "Thin-film solar cells: an overview," *Renew. energy*, vol. 8, no. 1–4 pt 1, pp. 69–92, 1996.

[3] D. Soni, P. Parsoya, B. K. Menariya, R. Vyas, and R. Ameta, "Photoelectrochemical cells," *Sol. Energy Convers. Storage Photochem. Modes*, vol. 414, no. November, pp. 29–53, 2015.

[4] National Energy Board, *Canada's Adoption of Renewable Power Sources: Energy Market Analysis*, no. May. 2017.

[5] K. P. Musselman and K. Poorkazem, *Fundamental Understanding of Solar Cells*. Elsevier Inc., 2019.

[6] "PN Junction Theory for Semiconductor Diodes." [Online]. Available: https://www.electronics-tutorials.ws/diode/diode_2.html. [Accessed: 11-Jul-2019].

[7] "The Difference Between Solar Cell, Module & Array | Samlex Solar." [Online]. Available: https://www.samlexsolar.com/learning-center/solar-cell-module-array.aspx. [Accessed: 06-Jul-2019].

[8] "Solar busbar and fingers explained - Novergy Solar." [Online]. Available: https://www.novergysolar.com/solar-busbar-fingers-explained/.

[9] Ossila, "Solar Cells: A Guide to Theory and Measurement – Ossila." [Online]. Available: https://www.ossila.com/pages/solar-cells-theory. [Accessed: 13-Jun-2019].

[10] C. Riordan and R. Hulstron, "What is an air mass 1.5 spectrum? (solar cell performance calculations)," in *IEEE Conference on Photovoltaic Specialists*, 1990, pp. 1085–1088.

[11] M. A. Green, "Solar cell fill factors: General graph and empirical expressions," *Solid State Electron.*, vol. 24, no. 8, pp. 788–789, 1981.

[12] T. Fuyuki and A. Kitiyanan, "Photographic diagnosis of crystalline silicon solar cells utilizing electroluminescence," *Appl. Phys. A Mater. Sci. Process.*, vol. 96, no. 1, pp. 189–196, 2009.

[13] T. Trupke, "Photoluminescence and Electroluminescence Characterization in Silicon Photovoltaics," *Photovolt. Sol. Energy*, pp. 322–338, 2017.

[14] J. Haunschild, M. Glatthaar, M. Kasemann, S. Rein, and E. R. Weber, "Fast series resistance imaging for silicon solar cells using electroluminescence," *Phys. Status Solidi - Rapid Res. Lett.*, vol. 3, no. 7–8, pp. 227–229, 2009.

[15] O. Kojima, Y. Harada, A. Hasegawa, T. Kita, T. Inoue, and W. Hu, "Intermediate band photovoltaics based on interband-intraband transitions using In0.53Ga0.47As/InP superlattice," *Prog. Photovoltaics Res. Appl.*, p. n/a-n/a, 2011.

[16] D. M. Tsai, S. C. Wu, and W. C. Li, "Defect detection of solar cells in electroluminescence images using Fourier image reconstruction," *Sol. Energy Mater. Sol. Cells*, vol. 99, pp. 250–262, 2012.

[17] I. Mora-Seró, G. Garcia-Belmonte, P. P. Boix, M. A. Vázquez, and J. Bisquert, "Impedance spectroscopy characterisation of highly efficient silicon solar cells under different light illumination intensities," *Energy Environ. Sci.*, vol. 2, no. 6, pp. 678–686, 2009.

[18] I. Mora-Seró *et al.*, "Recombination rates in heterojunction silicon solar cells analyzed by impedance spectroscopy at forward bias and under illumination," *Sol. Energy Mater. Sol. Cells*, vol. 92, no. 4, pp. 505–509, Apr. 2008.

[19] J. E. Garland, D. J. Crain, and D. Roy, “Impedance spectroscopy coupled with voltammetry for quantitative evaluation of temperature and voltage dependent parameters of a silicon solar cell,” *Sol. Energy*, vol. 85, no. 11, pp. 2912–2923, 2011.
[20] S. Kumar, P. K. Singh, and G. S. Chilana, “Study of silicon solar cell at different intensities of illumination and wavelengths using impedance spectroscopy,” *Sol. Energy Mater. Sol. Cells*, vol. 93, no. 10, pp. 1881–1884, 2009.
[21] P. Yadav, B. Tripathi, K. Pandey, and M. Kumar, “Investigating the charge transport kinetics in poly-crystalline silicon solar cells for low-concentration illumination by impedance spectroscopy,” *Sol. Energy Mater. Sol. Cells*, vol. 133, pp. 105–112, 2015.
[22] J. C. Jansen and J. C. Jansen, *Encyclopedia of Membranes*. 2015.
[23] P. Yadav, K. Pandey, B. Tripathi, and M. Kumar, “Investigation of interface limited charge extraction and recombination in polycrystalline silicon solar cell: Using DC and AC characterization techniques,” *Sol. Energy*, vol. 116, pp. 293–302, 2015.
[24] M. S. Suresh, “Measurement of solar cell parameters using impedance spectroscopy,” *Sol. Energy Mater. Sol. Cells*, vol. 43, no. 1, pp. 21–28, 1996.
[25] D. Chenvidhya, K. Kirtikara, and C. Jivacate, “PV module dynamic impedance and its voltage and frequency dependencies,” *Sol. Energy Mater. Sol. Cells*, vol. 86, no. 2, pp. 243–251, 2005.
[26] R. A. Kumar, M. S. Suresh, and J. Nagaraju, “Silicon (BSFR) solar cell AC parameters at different temperatures,” *Sol. Energy Mater. Sol. Cells*, vol. 85, no. 3, pp. 397–406, 2005.
[27] F. Fabregat-Santiago, J. Bisquert, G. Garcia-Belmonte, G. Boschloo, and A. Hagfeldt, “Influence of electrolyte in transport and recombination in dye-sensitized solar cells studied by impedance spectroscopy,” *Sol. Energy Mater. Sol. Cells*, vol. 87, no. 1–4, pp. 117–131, 2005.
[28] A. Guerrero and G. Garcia-Belmonte, “Recent advances to understand morphology stability of organic photovoltaics,” *Nano-Micro Lett.*, vol. 9, no. 1, 2017.
[29] A. Guerrero *et al.*, “Properties of Contact and Bulk Impedances in Hybrid Lead Halide Perovskite Solar Cells Including Inductive Loop Elements,” *J. Phys. Chem. C*, vol. 120, no. 15, pp. 8023–8032, 2016.
[30] S. K. Gupta, L. S. Pali, and A. Garg, “Impedance spectroscopy on degradation analysis of polymer/fullerene solar cells,” *Sol. Energy*, vol. 178, no. August 2018, pp. 133–141, 2019.
[31] K. P. Musselman, A. Marin, A. Wisnet, C. Scheu, J. L. MacManus-Driscoll, and L. Schmidt-Mende, “A novel buffering technique for aqueous processing of zinc oxide nanostructures and interfaces, and corresponding improvement of electrodeposited ZnO-Cu2O photovoltaics,” *Adv. Funct. Mater.*, vol. 21, no. 3, pp. 573–582, 2011.
[32] W. Peng, C. Aranda, O. M. Bakr, G. Garcia-Belmonte, J. Bisquert, and A. Guerrero, “Quantification of Ionic Diffusion in Lead Halide Perovskite Single Crystals,” *ACS Energy Lett.*, vol. 3, no. 7, pp. 1477–1481, 2018.
[33] M. Haro *et al.*, “Germanium coating boosts lithium uptake in Si nanotube battery anodes,” *Phys. Chem. Chem. Phys.*, vol. 16, no. 33, pp. 17930–17935, 2014.
[34] NREL, “Best Research-Cell Efficiency Chart | Photovoltaic Research | NREL,” 2019. [Online]. Available: https://www.nrel.gov/pv/cell-efficiency.html. [Accessed: 13-Jun-2019].
[35] F. H. Alharbi and S. Kais, “Theoretical limits of photovoltaics efficiency and possible improvements by intuitive approaches learned from photosynthesis and quantum coherence,” *Renew. Sustain. Energy Rev.*, vol. 43, pp. 1073–1089, 2015.

[36] T. Meng, “Inorganic Photovoltaic Solar Cells: Silicon and Beyond,” *Electrochem. Soc. Interface*, no. Winter, pp. 30–35, 2008.
[37] D. M. Powell, M. T. Winkler, H. J. Choi, C. B. Simmons, D. B. Needleman, and T. Buonassisi, “Crystalline silicon photovoltaics: A cost analysis framework for determining technology pathways to reach baseload electricity costs,” *Energy Environ. Sci.*, vol. 5, no. 3, pp. 5874–5883, 2012.
[38] E. J. Lee, D. S. Kim, and S. H. Lee, “Ni/Cu metallization for low-cost high-efficiency PERC cells,” *Sol. Energy Mater. Sol. Cells*, vol. 74, no. 1–4, pp. 65–70, 2002.
[39] A. W. Blakers, A. Wang, A. M. Milne, J. Zhao, and M. A. Green, “22.8% efficient silicon solar cell 22.8 % efficient siHcon solar cell,” *Cit. Appl. Phys. Lett. J. Appl. Phys. Appl. Phys. Lett.7% Effic. Appl. Phys. Lett. Appl. Phys. Lett. Phys. Lett*, vol. 551, no. 48, pp. 2998–602, 1989.
[40] S. Meier, S. Wasmer, A. Fell, N. Wöhrle, J. Greulich, and A. Wolf, “Efficiency Potential of p-type PERT vs. PERC Solar Cells,” *2018 IEEE 7th World Conf. Photovolt. Energy Conversion, WCPEC 2018 - A Jt. Conf. 45th IEEE PVSC, 28th PVSEC 34th EU PVSEC*, pp. 3578–3583, 2018.
[41] A. Hübner, A. G. Aberle, and R. Hezel, “Novel cost-effective bifacial silicon solar cells with 19.4% front and 18.1% rear efficiency,” *Appl. Phys. Lett.*, vol. 70, no. 8, pp. 1008–1010, 1997.
[42] L. Yang *et al.*, “High efficiency screen printed bifacial solar cells on monocrystalline CZ silicon,” *Prog. Photovoltaics Res. Appl.*, vol. 19, no. 3, pp. 275–279, May 2011.
[43] T. Dullweber *et al.*, “Bifacial PERC+ solar cells: status of industrial implementation and future perspectives,” 2017.
[44] F. H. Alharbi and S. Kais, “Theoretical limits of photovoltaics efficiency and possible improvements by intuitive approaches learned from photosynthesis and quantum coherence,” *Renew. Sustain. Energy Rev.*, vol. 43, pp. 1073–1089, 2015.
[45] X. Hu *et al.*, “Diagnosis of GaAs solar-cell resistance via absolute electroluminescence imaging and distributed circuit modeling,” *Energy*, vol. 174, pp. 85–90, 2019.
[46] M. Ravindiran and C. Praveenkumar, “Status review and the future prospects of CZTS based solar cell – A novel approach on the device structure and material modeling for CZTS based photovoltaic device,” *Renew. Sustain. Energy Rev.*, vol. 94, no. December 2017, pp. 317–329, 2018.
[47] M. T. Winkler, W. Wang, O. Gunawan, H. J. Hovel, T. K. Todorov, and D. B. Mitzi, “Optical designs that improve the efficiency of Cu2ZnSn(S,Se) 4 solar cells,” *Energy Environ. Sci.*, vol. 7, no. 3, pp. 1029–1036, 2014.
[48] S. Yun *et al.*, “New-generation integrated devices based on dye-sensitized and perovskite solar cells,” *Energy Environ. Sci.*, vol. 11, no. 3, pp. 476–526, 2018.
[49] T. D. Lee and A. U. Ebong, “A review of thin film solar cell technologies and challenges,” *Renew. Sustain. Energy Rev.*, vol. 70, no. September 2015, pp. 1286–1297, 2017.
[50] M. I. Asghar, J. Zhang, H. Wang, and P. D. Lund, “Device stability of perovskite solar cells – A review,” *Renew. Sustain. Energy Rev.*, vol. 77, no. February, pp. 131–146, 2017.
[51] C. Eames, J. M. Frost, P. R. F. Barnes, B. C. O’Regan, A. Walsh, and M. S. Islam, “Ionic transport in hybrid lead iodide perovskite solar cells,” *Nat. Commun.*, vol. 6, no. May, pp. 2–9, 2015.
[52] M. Lancaster, “Summary for Policymakers,” *Clim. Chang. 2013 - Phys. Sci. Basis*, vol. 53, no. 9, pp. 1–30, 1989.

[53] M. I. Oprea *et al.*, “Detection of potential induced degradation in c-Si PV panels using electrical impedance spectroscopy,” in *2016 IEEE 43rd Photovoltaic Specialists Conference (PVSC)*, 2016, no. 1, pp. 1575–1579.
[54] T. Lindner *et al.*, “Degradation of multicrystalline silicon solar cells and modules after illumination at elevated temperature,” *Sol. Energy Mater. Sol. Cells*, vol. 142, pp. 83–86, 2015.
[55] M. Nicolai, M. Zanuccoli, M. Galiazzo, M. Bertazzo, E. Sangiorgi, and C. Fiegna, “Simulation Study of Light-induced, Current-induced Degradation and Recovery on PERC Solar Cells,” *Energy Procedia*, vol. 92, pp. 153–159, 2016.
[56] C. E. Chan *et al.*, “Rapid Stabilization of High-Performance Multicrystalline P-type Silicon PERC Cells,” *IEEE J. Photovoltaics*, vol. 6, no. 6, pp. 1473–1479, 2016.
[57] S. Sharifi-Asl and D. D. Macdonald, “Electrochemical Impedance Spectroscopy,” *Dev. Electrochem. Sci. Inspired by Martin Fleischmann*, vol. 9781118694, no. 1, pp. 349–365, 2014.
[58] T. Tanahashi, N. Sakamoto, H. Shibata, and A. Masuda, “Localization and characterization of a degraded site in crystalline silicon photovoltaic cells exposed to acetic acid vapor,” *IEEE J. Photovoltaics*, vol. 8, no. 4, pp. 997–1004, 2018.
[59] H. Sakakura, M. Itagaki, and M. Sugiyama, “Estimation of defect activation energy around pn interfaces of Cu(In,Ga)Se2solar cells using impedance spectroscopy,” *Jpn. J. Appl. Phys.*, vol. 55, no. 1, 2016.
[60] M. Sugiyama, M. Hayashi, C. Yamazaki, N. B. Hamidon, Y. Hirose, and M. Itagaki, “Application of impedance spectroscopy to investigate the electrical properties around the pn interface of Cu(In,Ga)Se2 solar cells,” *Thin Solid Films*, vol. 535, no. 1, pp. 287–290, 2013.
[61] P. Hacke *et al.*, “System voltage potential-induced degradation mechanisms in PV modules and methods for test,” *Conf. Rec. IEEE Photovolt. Spec. Conf.*, no. July, pp. 000814–000820, 2011.
[62] W. Luo *et al.*, “Potential-induced degradation in photovoltaic modules: A critical review,” *Energy Environ. Sci.*, vol. 10, no. 1, pp. 43–68, 2017.
[63] W. Luo *et al.*, “Investigation of Potential-Induced Degradation in n-PERT Bifacial Silicon Photovoltaic Modules with a Glass/Glass Structure,” *IEEE J. Photovoltaics*, pp. 1–7, 2017.
[64] S. Pingel *et al.*, “Initial degradation of industrial silicon solar cells in solar panels,” *Proc. 25th Eur. Photovolt. Sol. Energy Conf.*, no. November 2014, pp. 4027–4032, 2010.
[65] W. Luo *et al.*, “Elucidating potential-induced degradation in bifacial PERC silicon photovoltaic modules,” *Prog. Photovoltaics Res. Appl.*, vol. 26, no. 10, pp. 859–867, 2018.
[66] J. Carolus, J. A. Tsanakas, A. van der Heide, E. Voroshazi, W. De Ceuninck, and M. Daenen, “Physics of potential-induced degradation in bifacial p-PERC solar cells,” *Sol. Energy Mater. Sol. Cells*, vol. 200, no. March, p. 109950, 2019.
[67] V. Naumann *et al.*, “Potential-induced degradation at interdigitated back contact solar cells,” *Energy Procedia*, vol. 55, pp. 498–503, 2014.
[68] W. Luo *et al.*, “Investigation of Potential-Induced Degradation in n-PERT Bifacial Silicon Photovoltaic Modules with a Glass/Glass Structure,” *IEEE J. Photovoltaics*, vol. 8, no. 1, pp. 16–22, Jan. 2018.
[69] B. J. Hallam *et al.*, “Hydrogen passivation of B-O defects in Czochralski silicon,” *Energy*

Procedia, vol. 38, no. Lid, pp. 561–570, 2013.
[70] M. H. Kang, J. Hong, I. Cooper, A. Ebong, B. Rounsaville, and A. Rohatgi, "Reduction in Light Induced Degradation (LID) in B-doped Cz-Si Solar Cells with SiCxNy Antireflection (AR) Coating," *J. Electrochem. Soc.*, vol. 158, no. 7, p. H724, 2011.
[71] R. H. Wills, F. E. Hall, S. J. Strong, and J. H. Wohlgemuth, "The AC photovoltaic module," in *Conference Record of the Twenty Fifth IEEE Photovoltaic Specialists Conference - 1996*, 1996, pp. 1231–1234.
[72] S. A. Chowdhury and M. Mourshed, "Off-grid electrification with solar home systems: An appraisal of the quality of components," *Renew. Energy*, vol. 97, pp. 585–598, 2016.
[73] C. H. Hsu and F. Mansfeld, "Concernng the conversion of the constant phase element parameter Y0into a capacitance," *Corrosion*, vol. 57, no. 9, pp. 747–748, 2001.
[74] C. Longo, A. F. Nogueira, and M. De Paoli, "Solid-State and Flexible Dye-Sensitized TiO 2 Solar Cells : a Study by Electrochemical Impedance Spectroscopy," *J. Phys. Chem. B*, vol. 106, pp. 5925–5930, 2002.
[75] S. N. Kane, A. Mishra, and A. K. Dutta, "Preface: International Conference on Recent Trends in Physics (ICRTP 2016)," *J. Phys. Conf. Ser.*, vol. 755, no. 1, 2016.
[76] J. P. Correa-Baena *et al.*, "Changes from Bulk to Surface Recombination Mechanisms between Pristine and Cycled Perovskite Solar Cells," *ACS Energy Lett.*, vol. 2, no. 3, pp. 681–688, 2017.
[77] Y. Y. Proskuryakov *et al.*, "Impedance spectroscopy of thin-film CdTe/CdS solar cells under varied illumination," *J. Appl. Phys.*, vol. 106, no. 4, 2009.
[78] B. Sopori *et al.*, "Understanding light-induced degradation of c-Si solar cells," in *2012 38th IEEE Photovoltaic Specialists Conference*, 2012, pp. 001115–001120.
[79] B. Sopori, Y. Zhang, and W. Chen, "Process Monitoring in Solar Cell Manufacturing," *9th Work. Cryst. Silicon Sol. Cell Mater. Process. Breckenridge, Color.*, no. October, pp. 1–10, 1999.
[80] A. Moehlecke and I. Zanesco, "Development of silicon solar cells and photovoltaic modules in Brazil: analysis of a pilot production," *Mater. Res.*, vol. 15, no. 4, pp. 581–588, 2012.
[81] J. Johnson, D. Schoenwald, S. Kuszmaul, J. Strauch, and W. Bower, "Creating Dynamic Equivalent PV Circuit Models With Impedance," *37th IEEE Photovolt. Spec. Conf.*, pp. 2328–2333, 2011.
[82] R. Wang, M. Mujahid, Y. Duan, Z. K. Wang, J. Xue, and Y. Yang, "A Review of Perovskites Solar Cell Stability," *Adv. Funct. Mater.*, vol. 1808843, pp. 1–25, 2019.
[83] J. A. Christians, P. A. Miranda Herrera, and P. V. Kamat, "Transformation of the excited state and photovoltaic efficiency of CH3NH3PbI3 perovskite upon controlled exposure to humidified air," *J. Am. Chem. Soc.*, vol. 137, no. 4, pp. 1530–1538, 2015.
[84] O. Malinkiewicz *et al.*, "Perovskite solar cells employing organic charge-transport layers," *Nat. Photonics*, vol. 8, no. 2, pp. 128–132, 2014.
[85] M. A. Haque, A. D. Sheikh, X. Guan, and T. Wu, "Metal Oxides as Efficient Charge Transporters in Perovskite Solar Cells," *Adv. Energy Mater.*, vol. 7, no. 20, pp. 1–23, 2017.
[86] P. P. González-Borrero *et al.*, "Optical band-gap determination of nanostructured WO3 film," *Appl. Phys. Lett.*, vol. 96, no. 6, pp. 4–6, 2010.
[87] G. W. Kim, G. Kang, K. Choi, H. Choi, and T. Park, "Solution Processable Inorganic–Organic Double-Layered Hole Transport Layer for Highly Stable Planar Perovskite Solar

Cells," *Adv. Energy Mater.*, vol. 8, no. 26, pp. 1–7, 2018.
[88] S. Masi *et al.*, "Room-temperature processed films of colloidal carved rod-shaped nanocrystals of reduced tungsten oxide as interlayers for perovskite solar cells," *Phys. Chem. Chem. Phys.*, vol. 20, no. 16, pp. 11396–11404, 2018.
[89] Z. Song, S. C. Watthage, A. B. Phillips, and M. J. Heben, "Pathways toward high-performance perovskite solar cells: review of recent advances in organo-metal halide perovskites for photovoltaic applications," *J. Photonics Energy*, vol. 6, no. 2, p. 022001, 2016.
[90] Z. Li, "Stable Perovskite Solar Cells Based on WO $_3$ Nanocrystals as Hole Transport Layer," *Chem. Lett.*, vol. 44, no. 8, pp. 1140–1141, 2015.
[91] J. Zhang, C. Shi, J. Chen, C. Ying, N. Wu, and M. Wang, "Pyrolysis preparation of WO3 thin films using ammonium metatungstate DMF/water solution for efficient compact layers in planar perovskite solar cells," *J. Semicond.*, vol. 37, no. 3, 2016.
[92] K. Mahmood, B. S. Swain, A. R. Kirmani, and A. Amassian, "Highly efficient perovskite solar cells based on a nanostructured WO<inf>3</inf>-TiO<inf>2</inf> core-shell electron transporting material," *J. Mater. Chem. A*, vol. 3, no. 17, pp. 9051–9057, 2015.
[93] K. Poorkazem and T. L. Kelly, "Improving the stability and decreasing the trap state density of mixed-cation perovskite solar cells through compositional engineering," *Sustain. Energy Fuels*, vol. 2, no. 6, pp. 1332–1341, 2018.
[94] R. Singh, P. K. Singh, B. Bhattacharya, and H. W. Rhee, "Review of current progress in inorganic hole-transport materials for perovskite solar cells," *Appl. Mater. Today*, vol. 14, pp. 175–200, 2019.
[95] P. Poodt *et al.*, "Spatial atomic layer deposition: A route towards further industrialization of atomic layer deposition," *J. Vac. Sci. Technol. A Vacuum, Surfaces, Film.*, vol. 30, no. 1, p. 010802, 2011.
[96] P. Poodt, J. van Lieshout, A. Illiberi, R. Knaapen, F. Roozeboom, and A. van Asten, "On the kinetics of spatial atomic layer deposition," *J. Vac. Sci. Technol. A Vacuum, Surfaces, Film.*, vol. 31, no. 1, p. 01A108, 2013.
[97] R. L. Z. Hoye and J. L. MacManus-Driscoll, *Atmospheric Pressure Spatial Atomic Layer Deposited Metal Oxides for Thin Film Solar Cells*. Elsevier Inc., 2019.
[98] D. Muñoz-Rojas *et al.*, "High-speed atmospheric atomic layer deposition of ultra thin amorphous TiO 2 blocking layers at 100 °C for inverted bulk heterojunction solar cells," *Prog. Photovoltaics Res. Appl.*, no. October 2011, p. n/a-n/a, Apr. 2013.
[99] C. L. Armstrong, "A Novel Atmospheric Deposition Method for Low Cost Photovoltaics," no. May, 2016.
[100] C. L. Dezelah IV *et al.*, "Atomic layer deposition of tungsten(III) oxide thin films from W 2(NMe2)6 and water: Precursor-based control of oxidation state in the thin film material," *J. Am. Chem. Soc.*, vol. 128, no. 30, pp. 9638–9639, 2006.
[101] J. Malm, T. Sajavaara, and M. Karppinen, "Atomic layer deposition of WO 3 thin films using W(CO) 6 and O 3 precursors," *Chem. Vap. Depos.*, vol. 18, no. 7–9, pp. 245–248, 2012.
[102] S. Zhuiykov *et al.*, "Atomic layer deposition-enabled single layer of tungsten trioxide across a large area," *Appl. Mater. Today*, vol. 6, pp. 44–53, 2017.
[103] S. Franke *et al.*, "Alumina films as gas barrier layers grown by spatial atomic layer deposition with trimethylaluminum and different oxygen sources," *J. Vac. Sci. Technol. A Vacuum, Surfaces, Film.*, vol. 35, no. 1, p. 01B117, 2017.

[104] C. Charles, N. Martin, M. Devel, J. Ollitrault, and A. Billard, "Correlation between structural and optical properties of WO3 thin films sputter deposited by glancing angle deposition," *Thin Solid Films*, vol. 534, pp. 275–281, 2013.
[105] I. Valyukh, S. Green, H. Arwin, G. A. Niklasson, E. Wäckelgård, and C. G. Granqvist, "Spectroscopic ellipsometry characterization of electrochromic tungsten oxide and nickel oxide thin films made by sputter deposition," *Sol. Energy Mater. Sol. Cells*, vol. 94, no. 5, pp. 724–732, 2010.
[106] M. Regragui, M. Addou, B. El Idrissi, J. C. Bernède, A. Outzourhit, and E. Ec-chamikh, "Effect of the annealing time on the physico-chemical properties of WO3 thin films prepared by spray pyrolysis," *Mater. Chem. Phys.*, vol. 70, no. 1, pp. 84–89, 2001.
[107] A. H. Jayatissa, S. Te Cheng, and T. Gupta, "Annealing effect on the formation of nanocrystals in thermally evaporated tungsten oxide thin films," *Mater. Sci. Eng. B Solid-State Mater. Adv. Technol.*, vol. 109, no. 1–3, pp. 269–275, 2004.
[108] S. H. Mohamed, H. A. Mohamed, and H. A. Abd El Ghani, "Development of structural and optical properties of WOx films upon increasing oxygen partial pressure during reactive sputtering," *Phys. B Condens. Matter*, vol. 406, no. 4, pp. 831–835, 2011.
[109] D. M. Dieter Mergel and and M. J. Martin Jerman, "Density and refractive index of thin evaporated films," *Chinese Opt. Lett.*, vol. 8, no. S1, pp. 67–72, 2010.
[110] K. Uchinokura, T. Sekine, and E. Matsuura, "Raman scattering by silicon," *Solid State Commun.*, vol. 11, no. 1, pp. 47–49, 1972.
[111] B. Pecquenard, H. Lecacheux, J. Livage, and C. Julien, "Orthorhombic WO3 formed via a Ti-stabilized WO3·1/3H2O phase," *J. Solid State Chem.*, vol. 135, no. 1, pp. 159–168, Jan. 1998.
[112] C. Balázsi and E. Ö. Zayim, "Preparation and Characterisation of $WO_3.1/3H_2O$ Thin Films," *Mater. Sci. Forum*, vol. 537–538, pp. 113–120, 2009.
[113] B. Gerand, G. Nowogrocki, J. Guenot, and M. Figlarz, "Structural study of a new hexagonal form of tungsten trioxide," *J. Solid State Chem.*, vol. 29, no. 3, pp. 429–434, 1979.
[114] H. S. Nalwa, *Nanostructured Materials and Nanotechnology*. Elsevier, 2016.
[115] L. Zhou *et al.*, "Enhanced planar perovskite solar cell efficiency and stability using a perovskite/PCBM heterojunction formed in one step," *Nanoscale*, vol. 10, no. 6, pp. 3053–3059, 2018.
[116] Y. N. Kim, H. G. Shin, J. K. Song, D. H. Cho, H. S. Lee, and Y. G. Jung, "Thermal degradation behavior of indium tin oxide thin films deposited by radio frequency magnetron sputtering," *J. Mater. Res.*, vol. 20, no. 6, pp. 1574–1579, 2005.
[117] X. Xu *et al.*, "Ultraviolet-ozone surface modification for non-wetting hole transport materials based inverted planar perovskite solar cells with efficiency exceeding 18%," *J. Power Sources*, vol. 360, pp. 157–165, 2017.
[118] Z. L. Tseng, L. C. Chen, C. H. Chiang, S. H. Chang, C. C. Chen, and C. G. Wu, "Efficient inverted-type perovskite solar cells using UV-ozone treated MoOx and WOx as hole transporting layers," *Sol. Energy*, vol. 139, pp. 484–488, 2016.